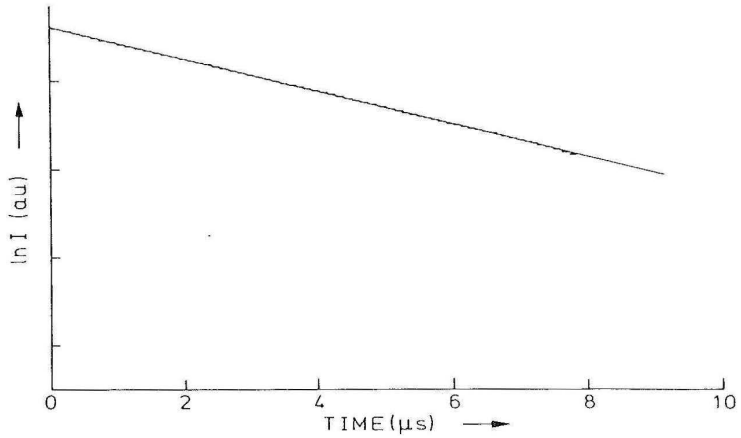

Fig. 3.6. Decay curve of the Eu^{2+} emission of SrB_4O_7 : Eu^{2+} at room temperature. The luminescence intensity I is plotted logarithmically versus the time after the excitation pulse. In agreement with Eq. (3.3) a straight line is found

recently been unravelled by modern experimental techniques. This example illustrates the process of relaxation, and simultaneously the power of the instrumental technique used, viz. femtosecond spectroscopy [5].

Consider as a specific example KCl, a very simple compound indeed. In Chapter 2, its lowest optical absorption band was mentioned to be due to the $3p^6 \rightarrow 3p^5 4s$ transition on the Cl^- ion. The excited state can be considered as a hole on the Cl^- ion (in the $3p$ shell) and an electron in the direct neighbourhood of the Cl^- ion, since the outer $4s$ orbital spreads over the K^+ ions. Now we consider what happens after the absorption process. The hole prefers to bind two Cl^- ions forming a V_K centre: this centre consists of a Cl_2^- pseudomolecule on the site of two Cl^- ions in the lattice. The electron circles around the V_K centre. In this way a self-trapped exciton is formed. An exciton is a state consisting of an electron and a hole bound together. By the relaxation process ($Cl^{-*} \rightarrow V_K.e$) the exciton has lowered its energy and is now trapped in the lattice.

Up till a few years ago it was generally assumed that the luminescence of KCl was due to self-trapped exciton recombination, i.e. the electron falls in the hole of the V_K center and the energy of the exciton is emitted as radiation. Recently, however, it was shown that the $V_K.e$ exciton can relax further: the Cl_2^- pseudomolecule moves to the lattice site of one Cl^- ion (this is called an H center), the electron to the other Cl^- site which is now vacant (this is the well-known F center). The new relaxed state is an F.H pair. It has a lower energy than the $V_K.e$ relaxed state. The several steps in the relaxation process are depicted in Fig. 3.7. As a matter of fact such a large relaxation results in an enormous Stokes shift (several eV's for alkali halides). After emission, the F.H configuration relaxes back to the ground state, i.e. $e_{Cl}.(Cl_2^-)_{Cl} \rightarrow$ 2ClдCl-. The subscript indicates the lattice site.

Vizio EX1018 Page 0050

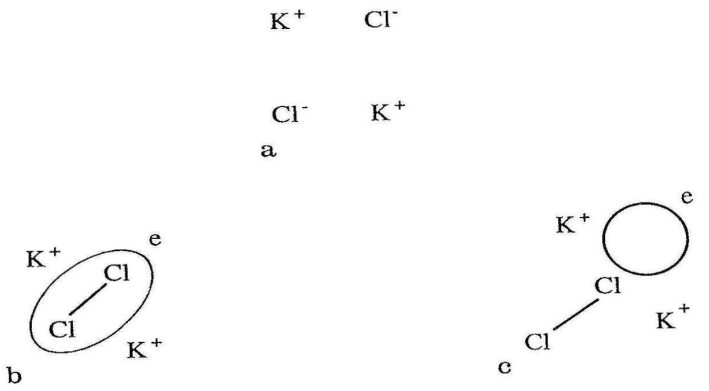

Fig. 3.7. Schematic representation of relaxed excited states in an alkali halide. *a*: ground state; *b*: self-trapped exciton consisting of a V_K centre and an electon; *c*: F.H pair centre. The electron is represented by its orbit (drawn line) marked by the letter *e*, the Cl_2^- pseudomolecule (i.e. the trapped hole) by Cl–Cl. See also text

This example shows clearly that the emission process is very different from the (simple) absorption process. For all details the reader is referred to the literature [5]. Finally we draw attention to the fact that the life time of the relaxed self-trapped exciton in the alkali halides is longer ($\sim 10^{-6}$s) than expected for an allowed transition ($10^{-7} - 10^{-8}$s). This is ascribed to the fact that the emitting state contains an amount of spin triplet character. Such a triplet state arises when the spins of the electron and the hole are oriented parallel. The emission transition becomes (partly) forbidden by the spin selection rule (see Chapter 2).

3.3.2 Rare Earth Ions (Line Emission)

The energy levels of the trivalent rare earth ions which arise from the $4f^n$ configuration are given in Figure 2.14. In a configurational coordinate diagram these levels appear as parallel parabolas ($\Delta R = 0$), because the $4f$ electrons are well shielded from the surroundings. Emission transitions yield, therefore, sharp lines in the spectra. Since the parity does not change in such a transition, the life time of the excited state is long ($\sim 10^{-3}$s).

The energy levels presented in Figure 2.14 are actually split by the crystal field. As a matter of fact the splitting is very small due to the shielding by the $5s^2$ and $5p^6$ electrons: whereas the crystal field strength in case of transition metal ions (d^n) is characteristically a few times 10 000 cm^{-1}, it amounts in the rare earth ions (f^n) a few times 100 $cm^{-}1$.

After these general considerations some special cases will be dealt with.

Vizio EX1018 Page 0051

a. Gd^{3+} $(4f^7)$

This ion has a half-filled $4f$ shell which gives a very stable $^8S_{7/2}$ ground state. The excited levels are at energies higher than 32 000 cm^{-1}. As a consequence the emission of Gd^{3+} is in the ultraviolet spectral region. The $^8S_{7/2}$ level (orbitally nondegenerate) cannot be split by the crystal field. This limits the low-temperature emission spectrum to one line, viz. from the lowest crystal field level of the $^6P_{7/2}$ level to $^8S_{7/2}$. However, usually the real spectrum consists of more than one line for several reasons.

- in the first place one usually observes weak vibronic transitions at energies below that of the electronic $^6P_{7/2} \rightarrow ^8S_{7/2}$ transition. In the vibronic transition two transitions occur simultaneously, viz. the electronic one (in this case $^6P_{7/2} \rightarrow ^8S_{7/2}$) and a vibrational one. Therefore, the energy difference between the electronic transition (in this context often called zero-phonon transition or origin) and a vibronic one yields the vibrational frequency of the mode which is excited in the emission process. In Figure 3.5 a vibronic line occurs in the Gd^{3+} emission spectrum at 1350 cm^{-1} below the electronic origin, which shows that vibrations of the borate group are involved. These vibronic transitions are observed in many rare-earth spectra (see, for example, Ref. [6].
- in the second place one may observe at higher energy than the electronic transition other transitions which are due to transitions from the higher crystal field levels of the $^6P_{7/2}$ level. Since the crystal field splitting is small, even at 4.2 K their population may be sizable. In Figure 3.8 we show as an example the emission spectrum of Gd^{3+} in $LuTaO_4$ at room temperature: there are four lines in the $^6P_{7/2} \rightarrow ^8S_{7/2}$ transition originating from the four crystal field levels of $^6P_{7/2}$, and, in addition, three lines belonging to the $^6P_{5/2} \rightarrow ^8S_{7/2}$ level which is also thermally populated at room temperature.
- if one excites with high enough energy (e.g. X rays) many more transitions are observed. An example is given in Figure 3.9. The composition (LaF_3 : Gd^{3+}) shows under X-ray excitation, in sequence of increasing energy, emission from the ^6P, ^6I, ^6D, and ^6G levels [7].

b. Eu^{3+} $(4f^6)$

The emission of this ion consists usually of lines in the red spectral area. These lines have found an important application in lighting and display (color television). These lines correspond to transitions from the excited $^5D_0$ level to the ^7F_J ($J = 0, 1, 2, 3, 4, 5, 6$) levels of the $4f^6$ configuration. Since the $^5D_0$ level will not be split by the crystal field (because $J = 0$), the splitting of the emission transitions yields the crystal-field splitting of the ^7F_J levels. This is illustrated in Figure 3.10. In addition to these emission lines one observes often also emission from higher ^5D levels, viz. $^5D_1$, $^5D_2$ and even $^5D_3$. The factors determining their presence or absence will be discussed in Chapter 4.

The $^5D_0$–^7F_J emission is very suitable to survey the transition probabilities of the sharp spectral features of the rare earths. If a rare-earth ion occupies in the crystal lattice a site with inversion symmetry, optical transitions between levels of the $4f^n$

Vizio EX1018 Page 0052

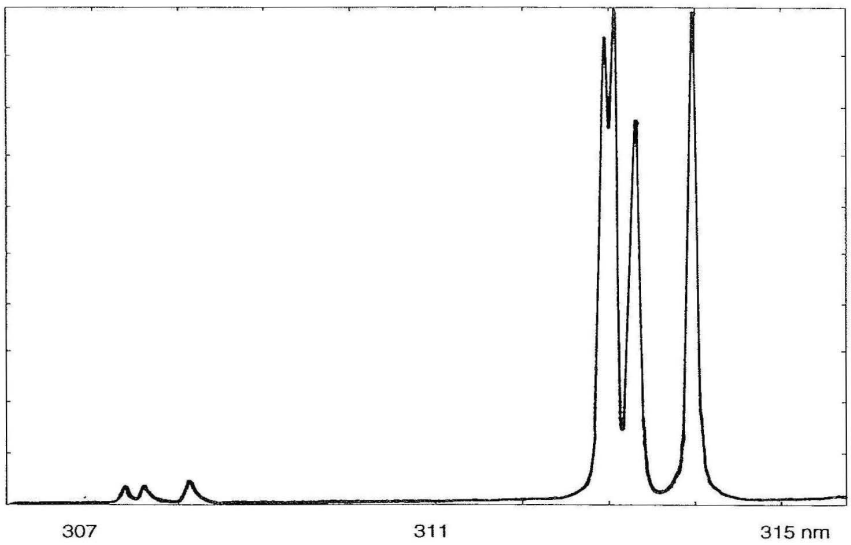

Fig. 3.8. Emission spectrum of the Gd^{3+} luminescence of $LuTaO_4$:Gd^{3+} at room temperature. The $^6P_{7/2} \rightarrow {}^8S_{7/2}$ transition shows four components (longer wavelength side), the $^6P_{5/2} \rightarrow {}^8S_{7/2}$ transition three (shorter wavelength side)

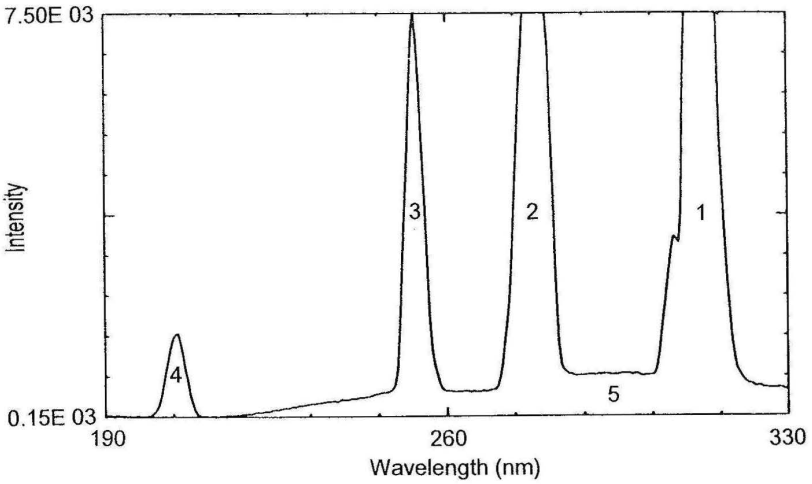

Fig. 3.9. The emission spectrum of the X-ray excited Gd^{3+} luminescence of LaF_3 : Gd^{3+}. Line 1 is the $^6P \rightarrow {}^8S$ transition, line 2 $^6I \rightarrow {}^8S$, line 3 $^6D \rightarrow {}^8S$, line 4 $^6G \rightarrow {}^8S$, whereas band 5 is the self-trapped exciton emission of LaF_3 (V_K type, see Sect. 3.3.1)

configuration are strictly forbidden as electric-dipole transition (parity selection rule). They can only occur as (the much weaker) magnetic-dipole transitions which obey the

Vizio EX1018 Page 0053

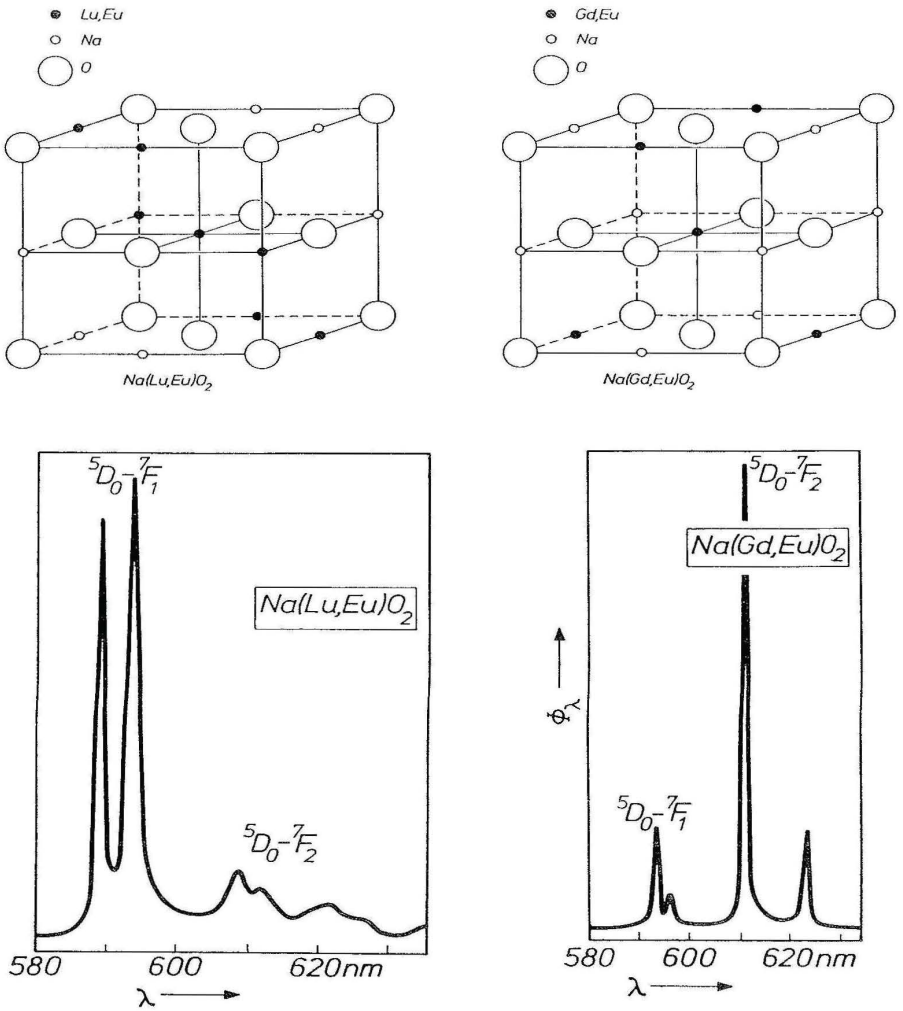

Fig. 3.10. The emission spectrum of Eu^{3+} in $NaLuO_2$ and $NaGdO_2$. In the $NaLuO_2 : Eu^{3+}$ spectrum the $^5D_0$–$^7F_1$ lines dominate, in the $NaGdO_2 : Eu^{3+}$ spectrum the $^5D_0$–$^7F_2$ lines. At the top of the Fig., a schematical presentation of the crystal structures of the host lattices is given. See also text

selection rule $\Delta J = 0, \pm 1$ (but $J = 0$ to $J = 0$ forbidden) or as vibronic electric-dipole transitions.

If there is no inversion symmetry at the site of the rare-earth ion, the uneven crystal field components can mix opposite-parity states into the $4f^n$-configurational levels (Sect. 2.3.3). The electric-dipole transitions are now no longer strictly forbidden and appear as (weak) lines in the spectra, the so-called forced electric-dipole transitions. Some transitions, viz. those with $\Delta J = 0, \pm 2$, are hypersensitive to this effect. Even for small deviations from inversion symmetry, they appear dominantly in the spectrum.

Vizio EX1018 Page 0054

We consider again Figure 3.10 for an illustration of these statements. The figure shows the emission spectra of $NaLuO_2 : Eu^{3+}$ and $NaGdO_2 : Eu^{3+}$. Both host lattices have the rocksalt structure, but with a different superstructure between mono- and trivalent metal ions. In $NaLuO_2$ the rare earth ions occupy a site with inversion symmetry. In $NaGdO_2$ the rare earth ions are octahedrally coordinated but due to the superstructure there is a small deviation from inversion symmetry.

In $NaLuO_2 : Eu^{3+}$ the $^5D_0$–$^7F_1$ emission transition is dominating. All other transitions occur only as very weak and broad lines. These are the vibronic transitions; the electronic origins are lacking. Since the starting level is $^5D_0$, the only possible magnetic-dipole transition is $^5D_0$–$^7F_1$, as observed experimentally. The trigonal crystal field at the rare earth site in $NaLuO_2$ splits this transition into two lines.

In $NaGdO_2 : Eu^{3+}$ the $^5D_0$–$^7F_2$ emission transition dominates, but other lines are also present. The Eu^{3+} case is so illustrative, because the theory of forced electric-dipole transitions [8] yields a selection rule in case the initial level has $J = 0$. Transitions to levels with uneven J are forbidden. Further $J = 0 \rightarrow J = 0$ is forbidden, because the total orbital momentum does not change. This restricts the spectrum to:
$^5D_0$–$^7F_1$, present as magnetic-dipole emission, but overruled by the forced electric-dipole emission,
$^5D_0$–$^7F_2$, a hypersensitive forced electric-dipole emission, which indeed is dominating,
$^5D_0$–$^7F_{4,6}$, weak forced electric-dipole emissions.

For applications it is required that the main emission is concentrated in the $^5D_0$–$^7F_2$ transition. This illustrates the importance of hypersensitivity in materials research.

c. Tb^{3+} $(4f^8)$

The emission of Tb^{3+} is due to transitions $^5D_4$–^7F_J which are mainly in the green. Often there is a considerable contribution to the emission from the higher-level emission $^5D_3$–^7F_J, mainly in the blue. Figure 3.11 gives an example of a Tb^{3+} emission spectrum. Since the J values, involved in the transitions, are high, the crystal field splits the levels in many sublevels which gives the spectrum its complicated appearance.

d. Sm^{3+} $(4f^5)$

The emission of Sm^{3+} is situated in the orange-red spectral region and consists of transitions from the $^4G_{5/2}$ level to the ground state $^6H_{5/2}$ and higher levels ^6H_J $(J > \frac{5}{2})$.

e. Dy^{3+} $(4f^9)$

The emission of Dy^{3+} originates from the $^4F_{9/2}$ level. Dominating are the transitions to $^6H_{15/2}$ ($\sim$ 470 nm) and $^6H_{13/2}$ ($\sim$ 570 nm). The latter one has $\Delta J = 2$ and is hypersensitive. The emission has a whitish color which turns to yellow in host lattices where hypersensitivity is pronounced.

Vizio EX1018 Page 0055

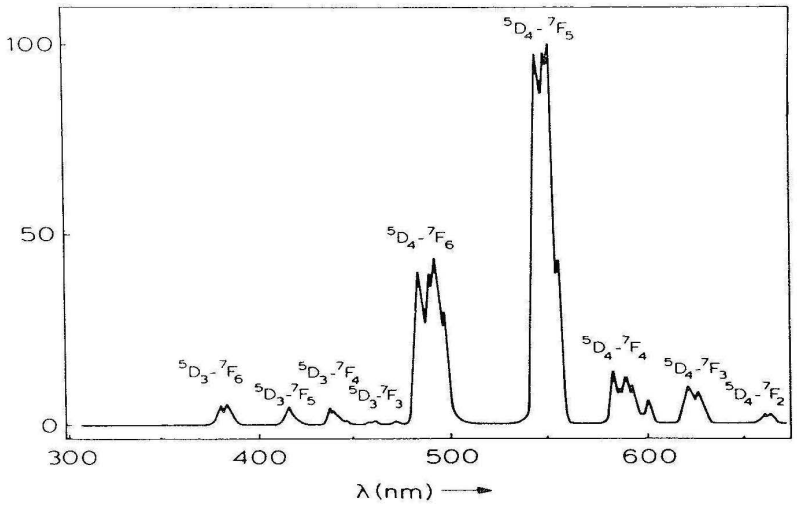

Fig. 3.11. The Tb^{3+} emission spectrum of $GdTaO_4 : Tb^{3+}$

f. Pr^{3+} $(4f^2)$

The emission color of Pr^{3+} depends strongly on the host lattice. If the emission originates from the $^3P_0$ level, it may be green ($^3P_0$–$^3H_4$) like in $Gd_2O_2S : Pr$, but red lines may also be strong ($^3P_0$–$^3H_6$, $^3F_2$) like in $LiYF_4 : Pr$. If the emission originates from the $^1D_2$ level, it is in the red and near-infrared. The factors determining whether emission occurs from $^3P_0$ or $^1D_2$ will be discussed later. The decay time of the $^3P_0$ emission is short for a rare earth ion (tens of μs). Not only is there no spin selection rule active, but also the $4f$ orbitals are probably more spread out in the lighter rare-earths (with lower nuclear charge) facilitating the mixing with opposite-parity states [9].

Rare-earth ion emission is not necessarily sharp line emission, as we will see now.

3.3.3 Rare Earth Ions (Band Emission)

Several rare earth ions show broad band emission. In this emission transition we are dealing with an electron which returns from a $5d$ orbital to the $4f$ orbital (see also Sect. 2.3.4). First we discuss trivalent ions (Ce^{3+}, Pr^{3+}, Nd^{3+}), later divalent ions (Eu^{2+}, Sm^{2+}, Yb^{2+}).

a. Trivalent Ions

The Ce^{3+} ion $(4f^1)$ is the most simple example, since it is a one-electron case. The excited configuration is $5d^1$. The $4f^1$ ground state configuration yields two levels, viz. $^2F_{5/2}$ and $^2F_{7/2}$, separated by some 2000 cm^{-1} due to spin-orbit coupling. The

Vizio EX1018 Page 0056

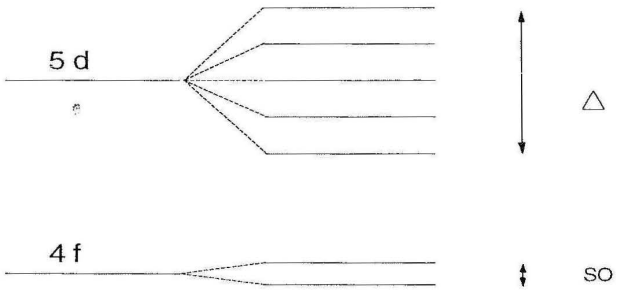

Fig. 3.12. The simplified energy level scheme of the Ce^{3+} ion ($4f^1$). On the left hand side only the $4f$level and the $5d$level are given without taking into account further interactions. On the right hand side the spin-orbit (SO) coupling has split the $4f$level into two components (about 2000 cm^{-1} apart), and the crystal field (Δ) has split the $5d$level into five crystal-field components spanning together some 15 000 cm^{-1}

$5d^1$ configuration is split by the crystal field in 2 to 5 components. The total splitting amounts to some 15 000 cm^{-1} (Fig. 3.12).

The emission occurs from the lowest crystal field component of the $5d^1$ configuration to the two levels of the ground state. This gives the Ce^{3+} emission its typical double-band shape (Fig. 3.13). Since the $5d \rightarrow 4f$transition is parity allowed and spin selection is not appropriate, the emission transition is a fully allowed one. The decay time of the Ce^{3+} emission is short, viz. a few ten ns. The decay time is longer if the emission is at longer wavelengths: 20 ns for the 300 nm emission of CeF_3, and 70 ns for the 550 nm emission of $Y_3Al_5O_{12}:Ce^{3+}$. It can be derived that for a given transition the decay time τ is proportional to the square of the emission wavelength λ [10]: $\tau \sim \lambda^2$.

The Stokes shift of the Ce^{3+} emission is never very large and varies from a thousand to a few thousand wave numbers (medium coupling case). The spectral position of the emission band depends on three factors:

- covalency (the nephelauxetic effect) which will reduce the energy difference between the $4f^1$ and $5d^1$ configurations
- crystal field splitting of the $5d^1$ configuration: a large low-symmetry crystal field will lower the lowest crystal-field component from which the emission originates.
- the Stokes shift.

Usually the Ce^{3+} emission is in the ultraviolet or blue spectral region, but in $Y_3Al_5O_{12}$ it is in the green and red (crystal-field effect), and in CaS in the red (covalency effect).

Under certain conditions $5d$–$4f$emission has also been observed for Pr^{3+} ($4f^2$) and Nd^{3+} ($4f^3$). For example, $LaB_3O_6:Pr^{3+}$ shows band emission around 260 nm and $LaF_3:Nd^{3+}$ around 175 nm. Due to the $\tau \sim \lambda^2$ relation, the decay time of the latter is only 6 ns [11]. However, these ions have an alternative way to emit, viz. by an emission transition in the $4f^n$ configuration.

Vizio EX1018 Page 0057

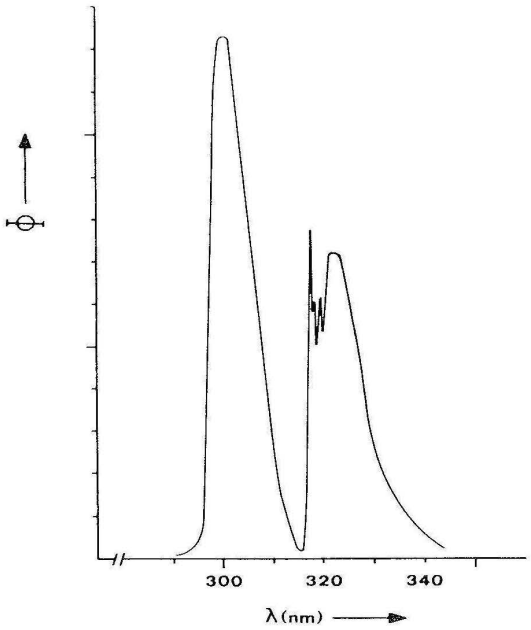

Fig. 3.13. The Ce^{3+} emission spectrum of $LiYF_4 : Ce^{3+}$ at 4.2 K. The two bands correspond to the transition from the lowest $5d$crystal-field component to the two components of the $4f$ground state. The longer wavelength component shows vibrational structure

b. Divalent Ions

In this group the most well-known and widely applied example is the Eu^{2+} $(4f^7)$ ion which shows a $5d \rightarrow 4f$ emission which can vary from long-wavelength ultraviolet to yellow. Its decay time is about 1 μs. This is due to the fact that the emitting level contains (spin) octets and sextets, whereas the ground state level (^8S from $4f^7$) is an octet, so that the spin selection rule slows down the optical transition rate.

The host lattice dependence of the emission colour of the Eu^{2+} ion is determined by the same factors as in the case of the Ce^{3+} ion. If the crystal field is weak and the amount of covalency low, the lowest component of the $4f^6 5d$ configuration of the Eu^{2+} ion may shift to such high energy, that the $^6P_{7/2}$ level of the $4f^7$ configuration lies below it. At low temperatures sharp-line emission due to the $^6P_{7/2} \rightarrow {}^8S_{7/2}$ transition occurs. This has been observed for quite a number of Eu^{2+}-activated compounds. As an example we can mention $SrB_4O_7 : Eu^{2+}$ [12].

Figure 3.14 gives the emission spectrum as a function of temperature. At 4.2 K there is line emission from $^6P_{7/2}$ (and a weak vibronic structure). At 35 K the thermally activated emission from the higher crystal-field components of $^6P_{7/2}$ appears, together with a broad band due to the $4f^6 5d \rightarrow 4f^7$ transition. This band has a zero-phonon line, indicated 0. At 110 K the band dominates.

Vizio EX1018 Page 0058

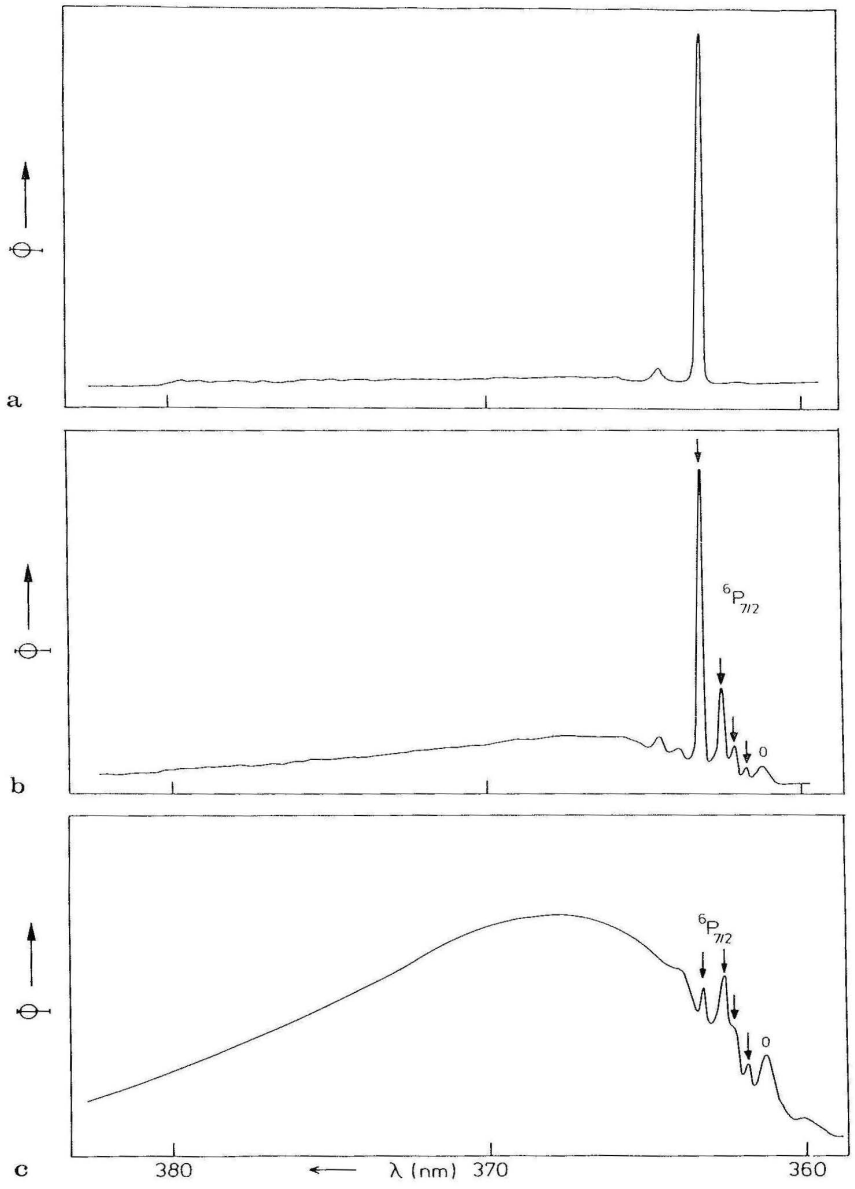

Fig. 3.14. The Eu^{2+} emission spectrum of $SrB_4O_7 : Eu^{2+}$ as a function of temperature. See also text. *a*: 4.2 K ($^6P_{7/2} \rightarrow {}^8S_{7/2}$ line emission); *b*: 35 K (line emissions, and broad band emission due to the $4f^6 5d \rightarrow 4f^7$ transition; *c*: 110 K (band emission dominates)

Vizio EX1018 Page 0059

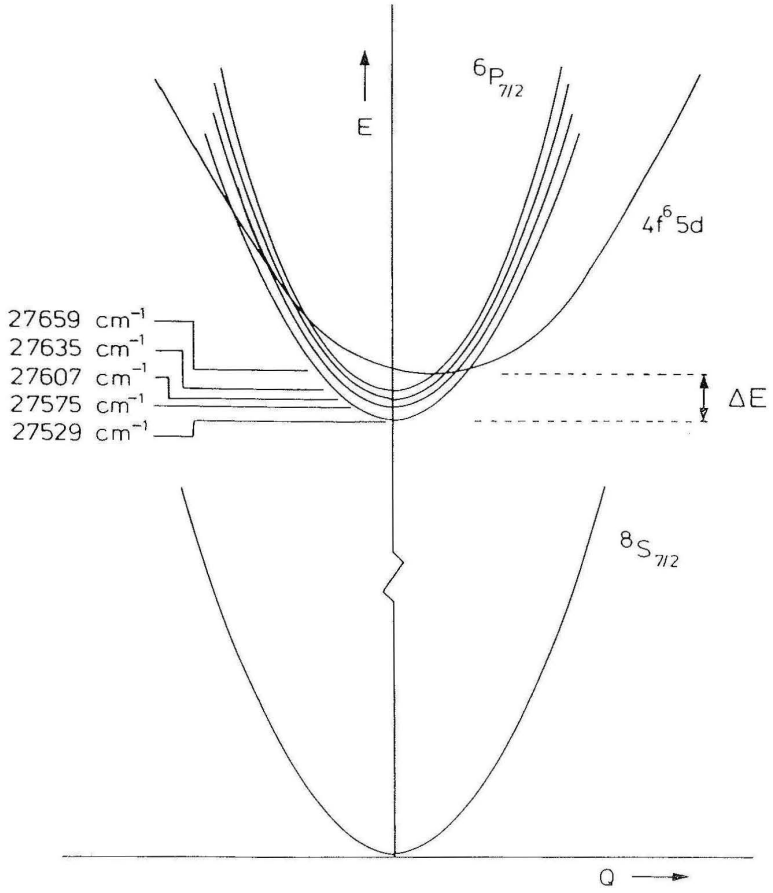

Fig. 3.15. Configurational coordinate model for Eu^{2+} in SrB_4O_7. Figs. 3.14 and 3.15 are derived from A. Meijerink, thesis, University Utrecht, 1990

Figure 3.15 gives the relevant configurational coordinate diagram with the four $^6P_{7/2}$ crystal-field levels and the lowest component of the $4f^6 5d$configuration (with a different equilibrium distance).

Finally Figure 3.16 gives the decay time of the Eu^{2+} emission in SrB_4O_7. At low temperatures it is 440 μs (parity forbidden $^6P \rightarrow {}^8S$ transition), but at higher temperatures it decreases rapidly due to the occurrence of the faster $5d \rightarrow 4f$emission.

The Sm^{2+} ion ($4f^6$) can show $5d \rightarrow 4f$emission in the red. However, if the lowest level of the $4f^5 5d$ configuration is at high energy, the intraconfigurational $4f^6$ emission is observed. This runs parallel with the case of Eu^{3+}, although the Sm^{2+} transitions are at a much longer wavelength.

The Yb^{2+} ($4f^{14}$) ion can only show one emission, viz. $4f^{13}5d \rightarrow 4f^{14}$. It is observed in the ultraviolet or blue. An example is given in Fig. 3.17. In the case of this ion the spin selection rule is of even more importance, since the observed decay times are very long for a $5d \rightarrow 4f$transition (a few ms, Ref. [13]).

Vizio EX1018 Page 0060

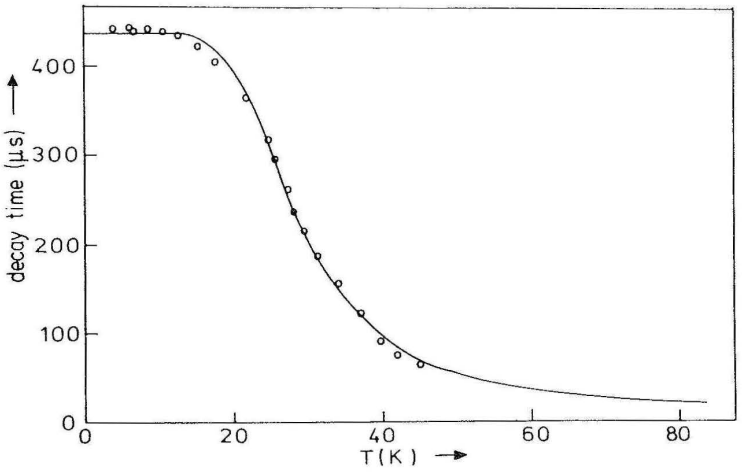

Fig. 3.16. Decay time of the Eu^{2+} emission of $SrB_4O_7 : Eu^{2+}$ as a function of temperature

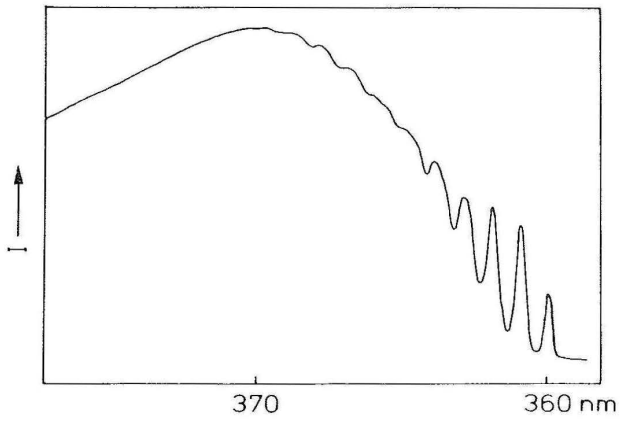

Fig. 3.17. The Yb^{2+} emission spectrum of $SrB_4O_7 : Yb^{2+}$ at 4.2 K

3.3.4 Transition Metal Ions

The luminescence of the transition metal ions will be discussed using the Tanabe-Sugano diagrams (Sect. 2.3.1). First we will consider ions which have played or still play an important role in luminescent materials, viz. Cr^{3+} and Mn^{4+} with d^3 configuration and Mn^{2+} with d^5 configuration. Then we will mention some ions which became more recently of interest. For a detailed account of this field the reader is referred to ref. [1].

Vizio EX1018 Page 0061

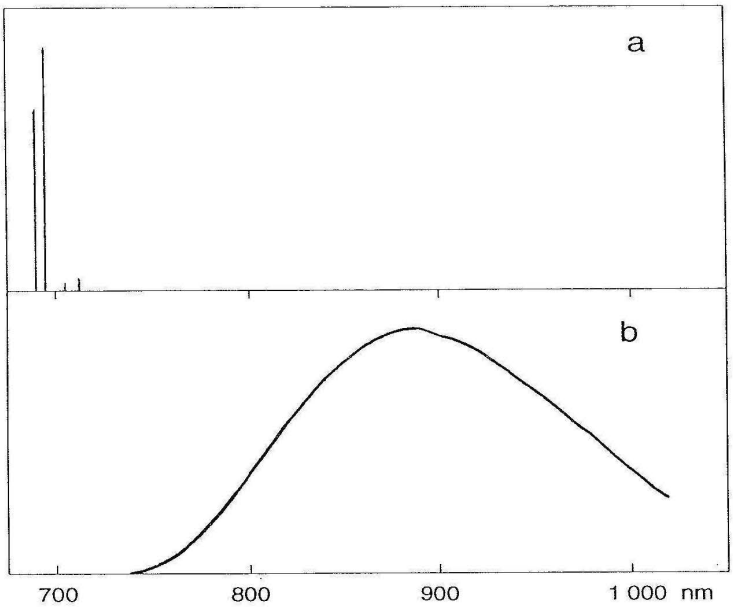

Fig. 3.18. Emission spectra of Cr^{3+}. *a*: $Al_2O_3:Cr^{3+}$ ($^2E \rightarrow {}^4A_2$ line emission); *b*: $Mg_4Nb_2O_9:Cr^{3+}$ ($^4T_2 \rightarrow {}^4A_2$ band emission)

a. Cr^{3+} (d^3)

The luminescence of Cr^{3+} in Al_2O_3 (ruby) has already been mentioned in Chapter 1. It formed the basis of the first solid state laser in 1960. This emission consists of two sharp lines (the so-called R lines) in the far red (see Fig. 3.18). Since it is a line, it must be due to the transition $^2E \rightarrow {}^4A_2$ (Fig. 2.9); generally speaking the emission of transition metal ions originates from the lowest excited state. The life time of the excited state amounts to some ms, because the parity selection rule as well as the spin selection rule apply. The emission line is followed by some weak vibronic transitions: obviously this emission transition belongs to the weak-coupling case.

Not always the ^2E level is the lowest excited state. For relatively low crystal fields the $^4T_2$ level is lower. In that case the emission changes character. It is now broad-band $^4T_2$–$^4A_2$ emission in the infrared with a decay time of $\sim$ 100 μs. As an example, Fig. 3.18 gives the emission spectrum of $Mg_4Nb_2O_9:Cr^{3+}$. This emission forms the basis of tunable infrared lasers. Figure 3.18 also illustrates how dramatic the crystal field influences the emission spectrum in the case of d^3 ions.

In $YAl_3B_4O_{12}:Cr^{3+}$, the emission at 4.2 K is $^2E \rightarrow {}^4A_2$, but at higher temperatures $^4T_2 \rightarrow {}^4A_2$. Although the ^2E level is below $^4T_2$, the latter can be thermally occupied at higher temperatures. Since the $^4T_2 \rightarrow {}^4A_2$ transition probability is higher than that of the $^2E \rightarrow {}^4A_2$ transition due to the spin selection rule, the $^4T_2$ emission rapidly dominates the emission spectrum.

The strength of the crystal field on the Cr^{3+} ion is therefore of imperative importance for its optical properties. Its color is red for high crystal field strength (ruby),

Vizio EX1018 Page 0062

and green for low crystal field strength. Its emission is a narrow line in the red in the former case, but a broad band in the near infrared in the latter. In some cases the $^4T_2 \rightarrow {}^4A_2$ emission band shows vibrational structure. There is not only a progression in the symmetric stretching mode ν_1, but also in ν_2 (see Fig. 3.4) indicating a tetragonally distorted excited state.

b. $Mn^{4+}(d^3)$

This ion is isoelectronic with Cr^{3+}, but the crystal field at the higher charged Mn^{4+} ion is stronger, so that the Mn^{4+} emission is always $^2E \rightarrow {}^4A_2$. Usually the vibronics are more intense than for Cr^{3+} [14].

c. $Mn^{2+}(d^5)$

The Mn^{2+} ion has an emission which consists of a broad band, the position of which depends strongly on the host lattice. The emission can vary from green to deep red. The decay time of this emission is of the order of ms. From the Tanabe-Sugano diagram (Fig. 2.10) we derive that the emission corresponds to the $^4T_1 \rightarrow {}^6A_1$ transition. This explains all the spectral properties: a broad band due to different slopes of the energy levels, a long decay time due to the spin selection rule, and a dependence of the emission color on the host lattice due to the dependence on crystal field. Tetrahedrally coordinated Mn^{2+} (weak crystal-field) usually gives a green emission, octahedrally coordinated Mn^{2+} (stronger crystal field) gives an orange to red emission.

d. Other d^n *ions*

The Ti^{3+} ion ($3d^1$) gives a broad-band emission in the near infrared due to the $^2E \rightarrow {}^2T_2$ transition. The titanium-sapphire laser is based on this emission.

The Ni^{2+} ion ($3d^8$) gives a complicated emission spectrum due to the appearance of emission transitions from more than one level. Luminescence from $KMgF_3 : Ni^{2+}$ appears in the near infrared ($^3T_2 \rightarrow {}^3A_2$), the red ($^1T_2 \rightarrow {}^3T_2$) and the green ($^1T_2 \rightarrow {}^3A_2$).

Güdel and coworkers, in recent years, have reported many near infrared emissions from transition metal ions with "unusual" valencies ($V^{2+}(3d^3)$, $V^{3+}(3d^2)$, $Ti^{2+}(3d^2)$, $Mn^{5+}(3d^2)$ [15]).

3.3.5 d^0 Complex Ions

Complexes of transition metal ions with a formally empty d shell show often intense broad-band emission with a large Stokes shift (10 000–20 000 cm^{-1}). Examples are VO_4^{3-}, NbO_6^{7-}, WO_4^{2-} and WO_6^{6-} [16]. The excited state is considered to be a charge-transfer state, i.e. electronic charge has moved from the oxygen ligands to the central metal ion. The real amount of charge transfer is usually small, but a considerable amount of electronic reorganisation occurs, in which electrons are promoted from

Vizio EX1018 Page 0063

Table 3.1. Decay times τ of some luminescent compounds with d^0 metal ions at 4.2 K.

Compound	τ (μs)
YVO_4	500
$KVOF_4$	33500
$Mg_4Nb_2O_9$	100
$CsNbOP_2O_7$	500
$CaMoO_4$	250
$CaWO_4$	330

bonding orbitals (in the ground state) to antibonding orbitals (in the excited state). The value of ΔR is large, the Stokes shift is large, and the spectral bands broad.

Especially the complexes with the lighter metal ions show long decay times of their emission. Table 3.1 gives some examples. Following early suggestions [16], Van der Waals et al. were able to prove that the emitting state is a spin triplet [17]. They showed also that the excited state is strongly distorted due to the Jahn-Teller effect. Here we meet another clear example of an excited state which is distorted relative to the ground state.

Octahedral complexes of this type have a smaller Stokes shift than the tetrahedral ones. The important consequences of this will be outlined in Chapter 5. Although not understood, certain structural configurations seem to promote efficient luminescence, for example, edge or face sharing of octahedral complexes (Li_3NbO_4, $Ba_3W_2O_9$), and the occurrence of one short metal-oxygen distance ($CsNbOP_2O_7$, $Ba_2TiOSi_2O_7$, $KVOF_4$ and vanadate on silica [18]).

Although it was believed for years that the emission spectra of these species were fully structureless, in recent years vibrational structure has been reported for several cases. A beautiful example is given in Fig. 3.19. This relates to vanadate on a silica surface. The progression is in a vibrational mode with a frequency of 950 cm^{-1}. This is the stretching vibration between vanadium and the oxygen pointing out of the silica surface.

The presence of ions with low-lying energy levels, for example ions with s^2 configuration, influence the d^0-complex luminescence drastically. For example, $CaWO_4:Pb^{2+}(6s^2)$ shifts its emission to longer wavelength relative to undoped $CaWO_4$ and the quenching temperature goes up. A nice example is $YVO_4:Bi^{3+}$ $(6s^2)$ which has a yellow emission, whereas YVO_4 has blue emission. Arguments have been given to ascribe the new emitting states to charge-transfer states in which the $6s$ electron is transferred to the empty $d$orbital (metal-to-metal charge transfer [19]).

3.3.6 d^{10} Ions

The emission transitions of ions with d^{10} configuration are of a complicated nature and are only partly understood. For clarity these ions are here divided into two classes,

Vizio EX1018 Page 0064

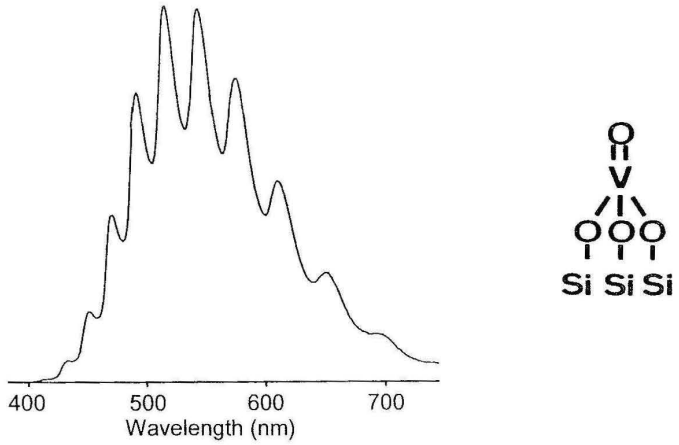

Fig. 3.19. Emission spectrum of the vanadate group on silica at 4.2 K

viz. the monovalent ones (Cu^+ and Ag^+) and the higher valent ones (for example Zn^{2+}, Ga^{3+}, Sb^{5+}, Te^{6+}).

a. Monovalent Ions

Complexes with monovalent d^{10} ions show often efficient emission at room temperature. For Cu^+ the reader can find a summary in Ref. [19]. The emission transition has been assigned to a $d^9s \rightarrow d^{10}$ transition, a ligand-to-metal charge-transfer transition, or a metal-to-ligand charge-transfer transition, depending on the ligands. In the mean time the first assignment has been put in doubt, since optically detected electron paramagnetic resonance measurements on the excited state of Cu^+ in NaF point to a very low spin density in the Cu 4*s* orbital [20]. As an alternative, the excited state may be thought of as a Cu^{2+} ion which distorts its surroundings due to the Jahn-Teller effect and an electron which has moved away from the hole in the *d* shell so that an exciton state is formed. This would be another example of an impressive relaxation after the absorption process.

The Stokes shift of the Cu^+ emission is usually large ($\geq 5000\ cm^{-1}$), indicating the strong-coupling scheme. About the Ag^+ ion less is known, but what is known shows a similarity with the Cu^+ data.

b. Higher Valent Ions

Luminescence from higher valent ions with d^{10} configuration has been questioned for a long time. Nowadays there exists strong evidence for such a luminescence. Examples are $Zn_4O(BO_2)_6$, $LiGaO_2$, $KSiSbO_5$ and $LiZrTeO_6$. The Stokes shifts are very large. Table 3.2 gives some spectral data [21].

The nature of this emission is not yet completely clear, but probably it is a charge-transfer transition, LMCT in absorption. However, also a transition on the oxygen ion ($2p^6 \rightarrow 2p^5 3s$) plays a role. Such an interpretation implies indeed a large

Vizio EX1018 Page 0065

Table 3.2. Some data on the luminescence of complexes with a central d^{10} metal ion. All values at 4.2 K and in cm^{-1}.

Compound	Complex	Emission max.	Excitation max.	Stokes shift
$Zn_4B_6O_{13}$	$Zn(II)O_4$	22.000	40.000	18.000
$LiGaO_2$	$Ga(III)O_4$	27.000	45.000	18.000
$KSbSiO_5$	$Sb(V)O_6$	21.000	41.500	20.500
Li_2ZrTeO_6	$Te(VI)O_6$	16.000	33.000	17.000

Table 3.3. Stokes shift of the Bi^{3+} emission in several host lattices [23].

Composition	Stokes shift (cm^{-1})
$Cs_2NaYCl_6 : Bi$	800
$ScBO_3 : Bi$	1800
$YAl_3B_4O_{12} : Bi$	2700
$CaLaAlO_4 : Bi$	7700
$LaOCl : Bi$	8500
$La_2O_3 : Bi$	10800
$Bi_2Al_4O_9$	16000
$Bi_4Ge_3O_{12}$	17600
$LaPO_4 : Bi$	19200
$Bi_2Ge_3O_9$	20000

amount of relaxation in the excited state and has been confirmed by molecular-orbital calculations.

Indeed the O^{2-} ion, when isolated in the lattice, can yield an emission of the type $2p^5 3s \rightarrow 2p^6$. Examples are $LiF : O^{2-}$, $CdF_2 : O^{2-}$ and $SrLa_2OBeO_4$. Since the $3s$ electron in the excited state has a widely spread orbital, this transition on oxygen, charge transfer in d^0 complexes and charge transfer in d^{10} complexes can be considered as three members of one family.

3.3.7 s^2 Ions

Ions with outer s^2 configuration are of large importance in the field of luminescence. In principle their spectroscopy is well understood [22]. The influence of the host lattice on these properties is drastic which fact is considerably less understood.

Well-known luminescent ions in this class are Tl^+, Pb^{2+}, Bi^{3+} (all $6s^2$), and Sn^{2+}, Sb^{3+} (both $5s^2$). The influence of the host lattice can be illustrated by comparing $Cs_2NaYCl_6 : Bi^{3+}$ where the emission consists of a narrow band with considerable vibrational structure and a small Stokes shift (800 cm^{-1}) and $LaPO_4 : Bi^{3+}$ where the emission consists of a broad band without any structure at all and with a large Stokes shift (19200 cm^{-1}). Table 3.3 shows that the Stokes shift varies one order of magnitude which is rather exceptional [23]. Figure 3.20 gives a spectral illustration.

Vizio EX1018 Page 0066

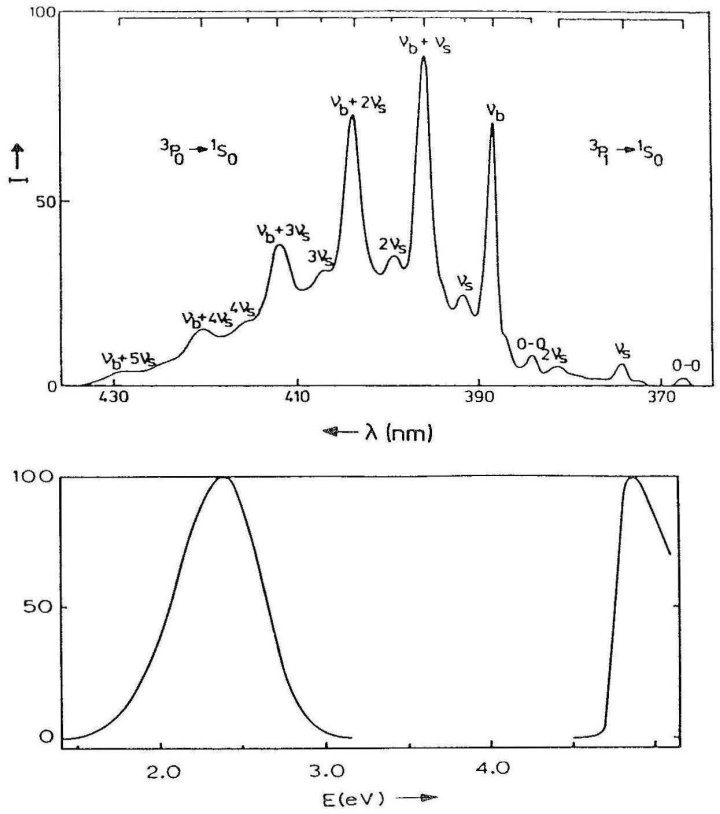

Fig. 3.20. Two different types of Bi^{3+} emission at 4.2 K. Top: $CaO:Bi^{3+}$; halfwidth of emission band about 1200 cm^{-1}; the vibrational structure has been interpreted using a stretching (νs) and a bending (νb) vibration. Bottom: $Bi_2Ge_3O_9$, halfwidth of emission band about 5000 cm^{-1}. The bottom spectrum also gives the excitation spectrum (right hand side), illustrating the enormous Stokes shift ($\sim$ 20 000 cm^{-1})

This large variation has been ascribed to the amount of space available for the Bi^{3+} ion in the lattice. The small Stokes shift case is only observed for Bi^{3+} in six coordination. The Bi^{3+} ion is too large for six coordination and has no possibility to relax to a different equilibrium distance. In a large site the situation is different. It has been proposed that in the ground state the Bi^{3+} goes off center when there is enough space. In this way it obtains its preferred asymmetrical coordination. This is an example of the pseudo Jahn-Teller effect [24]. After optical absorption the ion relaxes to the center of the coordination polyhedron. Due to this large relaxation a large Stokes shift results. Actually there is not much difference between two compounds like $CaWO_4$ and $Bi_4Ge_3O_{12}$ as far as their luminescence is concerned: both show after short-wave ultraviolet excitation an enormous amount of relaxation in the excited state where the bonding conditions have changed considerably in comparison to the ground state.

Evidence for this description of the relaxation of the Bi^{3+} ion stems from EXAFS measurements on $LaPO_4:Bi^{3+}$: in the ground state the Bi^{3+} coordination is more asymmetrical than the La^{3+} coordination. Another piece of evidence is the lumines-

Vizio EX1018 Page 0067

cence of bismuth compounds like $Bi_4Ge_3O_{12}$ where the ground state coordination is known from crystallographic data. Compounds of this type luminesce with large Stokes shifts. The same holds for some lead compounds ($PbAl_2O_4$, $PbGa_2O_4$).

After having presented the wide range of luminescence properties of s^2 ions, we now turn our attention to the excited state. The excited *sp* configuration yields a lower ^3P state. This state may undergo two different types of interaction, viz. spin-orbit (SO) interaction and Jahn-Teller (JT) (electron-lattice) interaction. The SO interaction will split the ^3P state into the $^3P_0$, $^3P_1$ and $^3P_2$ levels. The strength of this interaction increases with nuclear charge, i.e. from $4s^2$ to $6s^2$ ions and from low to high charge. The JT effect causes also a splitting of the ^3P state due to coupling of this state with vibrational modes. For octahedral coordination these are the ν_2 and ν_5 modes of the MX_6 octahedron (M = s^2 ion, X = ligand). If the SO coupling is strong, the influence of the JT effect is expected to decrease.

The importance of the JT effect in the spectroscopy of s^2 ions can be easily observed from the splitting of the $^1S_0 \rightarrow {}^3P_1$, $^1P_1$ absorption transitions [22]. The consequences for the emission are even more drastic. In some cases two emission bands are observed. An example is given in Figure 3.21, where the emission of $YPO_4 : Sb^{3+}$ is given as a function of temperature. The two emissions arise from different minima on the potential energy surface of the relaxed excited state. Figure 3.22 gives a schematic representation. At low temperatures the X minimum which is populated by optical excitation emits. At higher temperatures the barrier can be overcome and emission from the T minimum is also observed. At still higher temperatures, thermal equilibrium between the two minima occurs and the X emission reappears. The occurrence of two different minima depends strongly on the ratio between SO and JT couplings and the site symmetry of the s^2 ion.

Above it was already mentioned that the Te^{4+} ion shows a vibrational progression in its emission spectrum. This has to be ascribed to coupling with the ν_2 mode and indicates a tetragonally distorted excited state. This is also a manifestation of the JT interaction.

In the case of the $6s^2$ ions the SO interaction is so strong that the emission can be interpreted in terms of the SO-split levels $^3P_1$ and $^3P_0$. The vibrational progression in the emission band, if present, is always due to coupling with the symmetric ν_1 mode. At low temperatures the decay time becomes very long (ms range), since the $^3P_0 \rightarrow {}^1S_0$ emission is strongly forbidden. At higher temperatures the $^3P_1$ level becomes thermally occupied and the decay time becomes much faster. This runs parallel with the discussion above on the Eu^{2+} ion (see Fig. 3.16).

Three contributions to the Stokes shift of s^2 ion emission have to be taken into account [25]. This must be done in a multidimensional configurational coordinate diagram and is mentioned here as an illustration of the complicated nature of this emission and, especially, of the relaxation into the excited state. We will restrict ourselves to octahedral coordination.

a. a shift along the Jahn-Teller active modes ν_2 and ν_5. According to the Te^{4+} emission, the shift along ν_2 dominates. This corresponds to a tetragonal distortion.

b. a shift along the symmetrical ν_1 mode. This corresponds to a symmetrical expansion.

Vizio EX1018 Page 0068

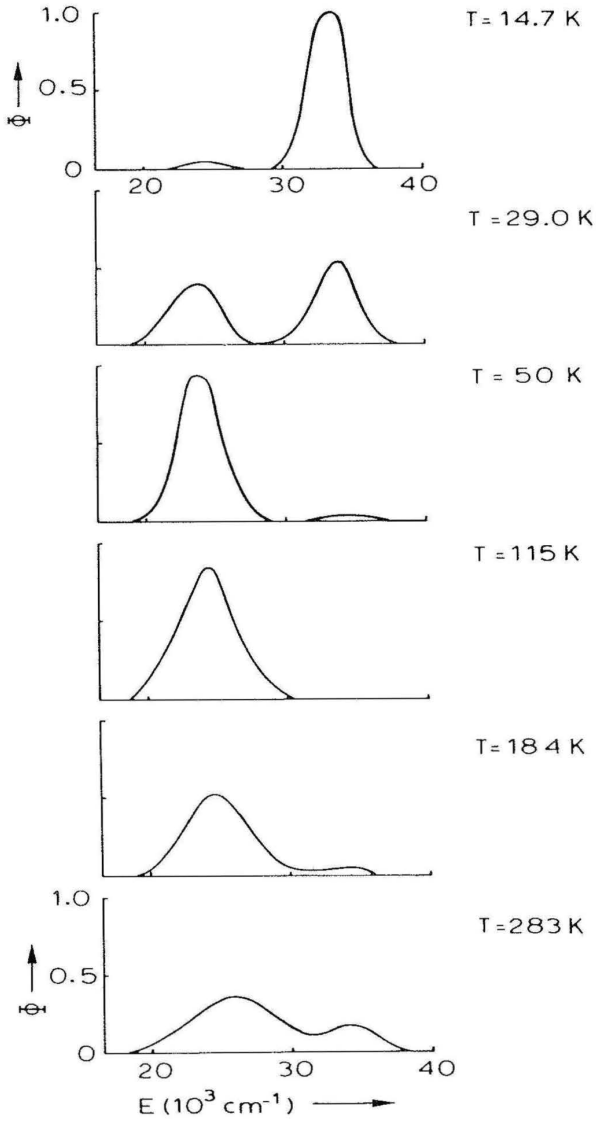

Fig. 3.21. The emission spectrum of $YPO_4 : Sb^{3+}$ as a function of temperature. See also Fig. 3.22. At low temperatures mainly UV emission is observed, at higher temperatures the blue emission dominates, and at room temperature the UV emission reappears. From E.W.J.L. Oomen, thesis, University Utrecht, 1987

Vizio EX1018 Page 0069

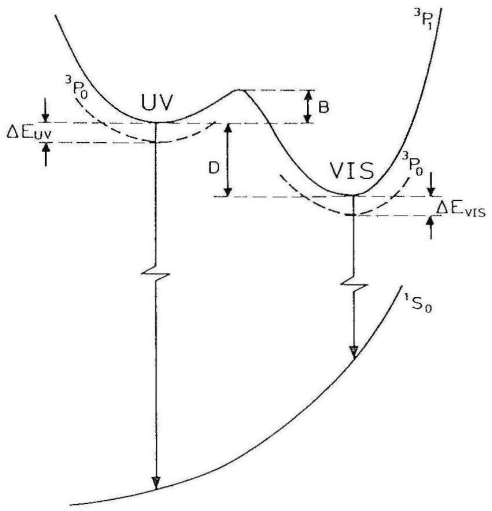

Fig. 3.22. Schematic configurational coordinate diagram for $YPO_4 : Sb^{3+}$. The potential energy curve of the excited state contains two minima. Optical excitation feeds the UV-emitting minimum. At low temperatures UV emission occurs. When the barrier B can be passed thermally, blue emission appears. When thermal back transfer over the barrier $\Delta E + B$ becomes possible, the UV emission reappears

c. a shift along a mode with t_{1u} symmetry which mixes the electronic ground state with excited T_{1u} states (pseudo Jahn-Teller effect). This distorts the ground state, often trigonally.

In the Te^{4+} emission the contribution **a** dominates which is probably true for many $4s^2$ and $5s^2$ ions (JT coupling in the excited state dominating). In the emission of $6s^2$ ions on a small site the contribution **b** dominates. For $6s^2$ ions with a distorted ground state the contribution **c** dominates. However, there are all types of mixtures possible, which makes the s^2 ion emission so complicated.

3.3.8 The U^{6+} ion

Hexavalent uranium played a role in the early experiments by Stokes (1852). This ion can show an intense green luminescence. Originally it was thought that this luminescence could only be obtained from the uranyl (UO_2^{2+}) ion. Later it appeared that octahedral UO_6^{6-} and tetrahedral UO_4^{2-} luminesce as well. The emission color of the latter complex is red. In NaF the introduction of U^{6+} even leads to a whole family of luminescent centers with a general formula $[UO_{6-x}Fx]^{(6-x)-}$ ($x = 0, 1, 2, 3$). These are all octahedral and replace the NaF_6 octahedron in the crystal lattice. Figure 3.23 gives as an example of uranate luminescence the emission spectrum of $Ba_2ZnWO_6 : U^{6+}$.

The U^{6+} ion can formally be considered as a $5f^0$ ion. Indeed the optical transitions involved are of the charge-transfer type. Figure 3.23 shows that we have here the

Vizio EX1018 Page 0070

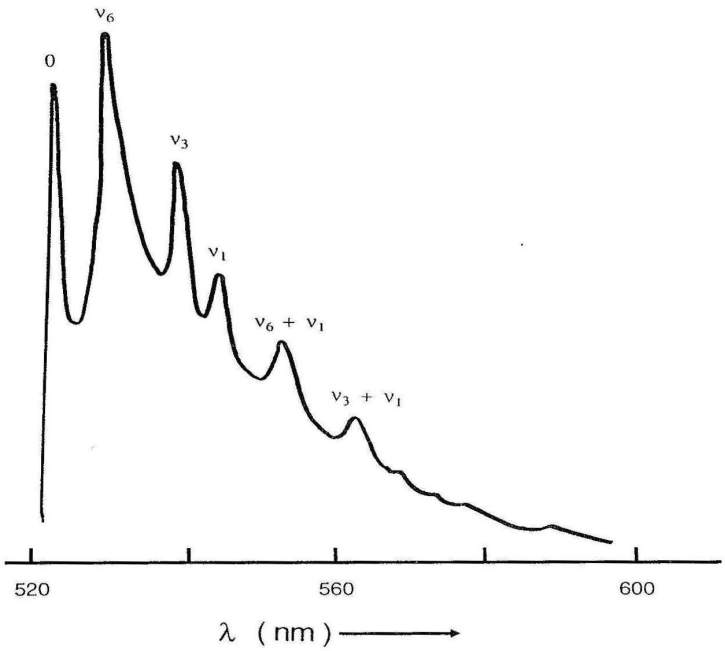

Fig. 3.23. The emission spectrum of $Ba_2ZnWO_6 : U^{6+}$ at 4.2 K. The zero-phonon line is indicated by O, the vibronic lines are indicated by the octahedral vibrational modes with which the coupling with the electronic transition takes place

intermediate-coupling case. An extensive study of the uranyl spectroscopy has been made by Denning [26].

3.3.9 Semiconductors

This book does not aim to treat semiconductors in any detail. However, we have several reasons to mention, at least superficially, emission from semiconductors. These are:

- luminescent semiconductors form an important class of materials with applications in the display field (television, electroluminescence of thin layers, light-emitting diodes)
- compounds made up of the luminescent centers discussed above are sometimes semiconductors, and sometimes not. In this way we meet the interesting boundary regime between semiconductors and insulators.

This section will discuss the following topics: "classic" semiconductors with near-edge and deep-center emission, and subsequently compounds in the boundary regime between semiconductors and insulators. For a more detailed treatment of the first topic, the reader is referred to Ref. [27]; for the second topic we follow a treatment sketched before in Ref. [23].

Vizio EX1018 Page 0071

a. Semiconductors

Semiconductors are characterized by a valence band and a conduction band separated by an energy gap E_g of a few eV. Excitation of the luminescence occurs by exciting electrons to the empty conduction band leaving holes in the completely filled valence band. Emission occurs by electron-hole recombination. However, emission due to recombination of free electrons and holes is exceptional. Usually recombination occurs close to or at defects in the crystal lattice. Phenomenologically it has been the practice to distinguish edge emission, i.e. emission close to the energy E_g, and deep-center emission, i.e. emission at an energy considerably lower than E_g.

Edge emission is due to exciton recombination (Sect. 3.3.1). Usually this emission is due to bound excitons, i.e. an exciton of which either the electron or the hole is trapped at an imperfection in the lattice. The elucidation of the nature of this imperfection is often a difficult task. As an example of such an emission we can mention the exciton emission of GaP : N. Nitrogen is an isoelectronic dopant (on phosphorous sites). The exciton is bound to this nitrogen impurity before it decays. The emission is situated at about 0.02 eV below E_g. Another semiconductor for which exciton emission has been thoroughly studied is CdS.

Another type of recombination in semiconductors is donor-acceptor pair emission. In this type of emission an electron trapped at a donor and a hole trapped at an acceptor recombine. Again GaP is a very nice example (Fig. 3.24). The donor-acceptor pair emission in this figure is due to a S_P–Zn_{Ga} pair transition. The lines are due to the fact that the distance between the donor S_P and the acceptor Zn_{Ga} varies due to their statistical distribution over the lattice, so that the binding energy of electron and hole varies with the distance between the centers where they are trapped.

Also in other semiconductors such donor-acceptor pair emissions have been found. A well-known example is ZnS : Cu,Al where Al_{Zn} is the donor and Cu_{Zn} the acceptor. This material is used as the green-emitting phosphor in color television tubes. The blue emission of ZnS : Al is due to recombination in an associate consisting of a zinc vacancy (acceptor) and Al_{Zn} (donor). Since these centres occur as coupled defects, their distance is restricted to one value only (this is sometimes called a molecular center). Due to strong electron-lattice coupling the emissions from ZnS consist of broad bands.

The emissions of ZnS : Al and ZnS : Cl are practically the same. In both cases we have the same center (although chemically different): an associate of a donor (Al_{Zn} or Cl_S) and an acceptor (V_{Zn}). This illustrates that not the chemical nature of the center determines its luminescence properties, but its position in the forbidden zone. This is very different from the centers discussed in previous sections. Actually reduction of E_g (for example by moving from ZnS to ZnSe) shifts all emissions to a correspondingly lower energy.

Other possibilities for radiative recombination are a free hole that recombines with a trapped electron (Lambe-Klick model) or a free electron that recombines with a trapped hole (Schön-Klasens model). The trapped charge carriers may occupy deep traps, so that the emitted energy is considerably less than E_g. Figure 3.25 reviews the possibilities mentioned here for radiative recombination in a semiconductor.

Vizio EX1018 Page 0072

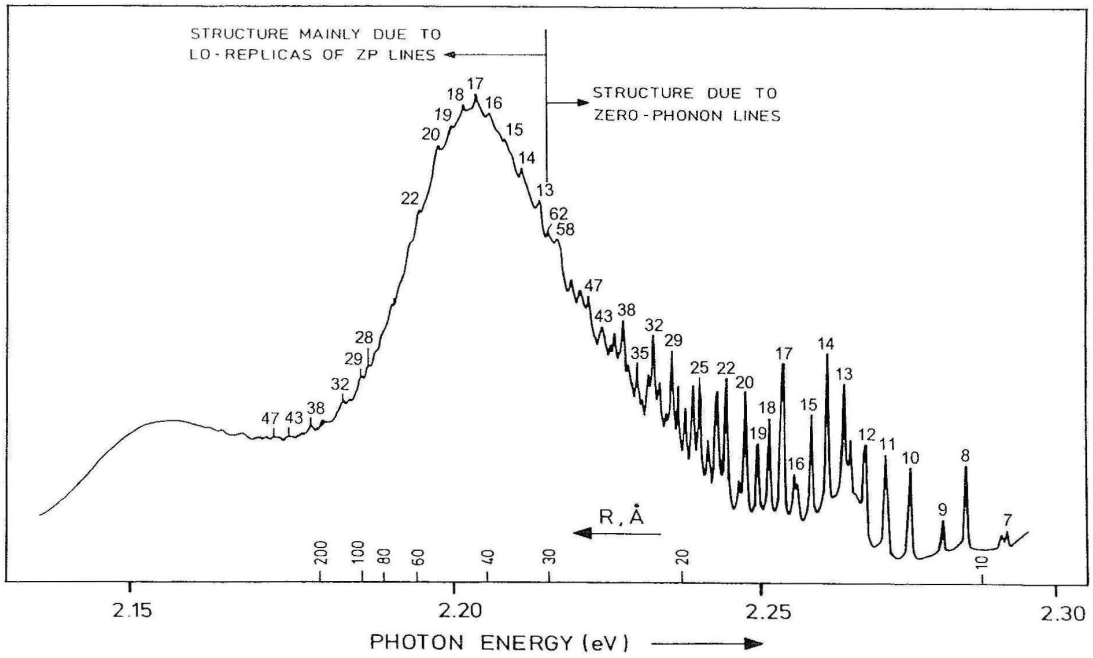

Fig. 3.24. The S_P–Zn_{Ga} donor-acceptor pair emission in GaP at 1.6 K. At the bottom R indicates the donor-acceptor distance of the relevant emitting pair. The lines are indicated by their shell number (shell 1 means nearest-neighbour pairs, etc.). On the right-hand side we see the zero-phonon lines of the individual lines; on the left-hand side we see mainly vibronic lines (in the semiconductor field often called replicas) due to coupling with host-lattice modes. Modified from A.T. Vink, thesis, Technical University Eindhoven, 1974

b. On the Boundary Between Semiconductors and Insulators

The greater part of this chapter has been based on the configurational coordinate model. The luminescent centers were classified according to the value of the Huang-Rhys parameter S (weak, medium or strong coupling). This implies that the interaction between electronic and vibrational transitions was dominant. The system was assumed to have localized electrons.

This neglects another important factor in solids, viz. delocalization. This was in fact only used above when introducing the energy band scheme (in the case of semiconductors). Localization and delocalization are competitive effects as will be shown now.

Consider a system of luminescent centers, each with a two-level energy scheme, with a large distance between the centers. If the distance is decreased, two effects may occur, viz.

– the excited state couples strongly with the vibrations of the system, so that strong relaxation occurs after excitation. This brings the system out of resonance with its neighbours, and promotes localization. This situation is described by the configurational coordinate diagram.

Vizio EX1018 Page 0073

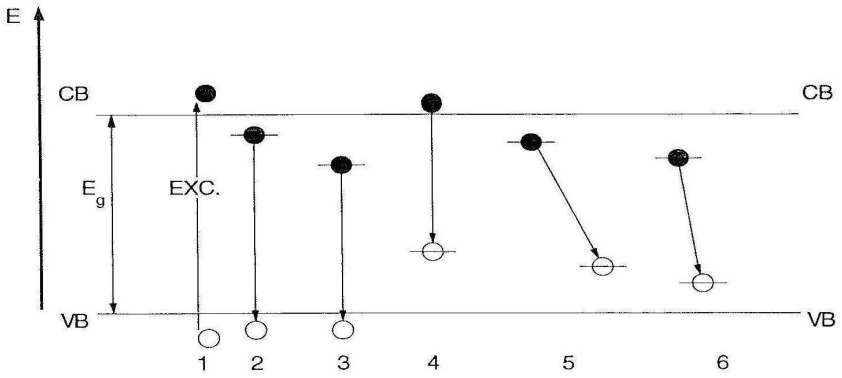

Fig. 3.25. Emission transitions in a semiconductor (schematical representation). The band gap E_g separates the valence band (VB) and the conduction band (CB). Excitation over the band gap (*1*) creates electrons in CB and holes in VB. Optical recombination is shown in processes 2–6: (*2*): a free hole recombines with an electron trapped in a shallow trap level (near-edge emission); (*3*): the same with a deep electron-trapping level; (*4*): a free electron recombines with a trapped hole; (*5*): donor-acceptor pair emission; (*6*): electron-hole recombination in an associate of a donor and an acceptor

– the wave functions of the levels of the individual centers overlap considerably and energy-band formation occurs. This promotes delocalization. The situation is described with the energy band model. Figure 3.26 shows this schematically. The top of the triangle presents the centres at large distance (no interaction). Along the left-hand leg delocalization increases, along the right-hand leg localization. The basis of the triangle presents the solid state with semiconductors with mobile charge carriers on the left-hand side, and insulators on the right-hand side. Along the basis the amount of localization increases from left to right. Simultaneously spectral band width and Stokes shift increases. The semiconductor in this definition is completely pure and should only show free-exciton emission as a sharp line very close to E_g, the band gap energy.

Here are some illustrative examples. The intraconfigurational $4f^n$ transitions of the rare-earth ions are located at the apex of the triangle, because they present, even in a solid, a nearly isolated system.

The compounds $CaWO_4$ and $Bi_4Ge_3O_{12}$ with large relaxation in the excited state and strongly Stokes-shifted emission are on the right-hand side of the base of the triangle (strong electron-lattice coupling, high S value).

Free exciton emission has been observed for $Cs_3Bi_2Br_9$ and TiO_2. They are placed on the left-hand side of the base. This is also true for $CsVO_3$, whereas YVO_4 is on the right-hand side.

The latter example illustrates another difference between compounds on the left- and right-hand side of the basis. The semiconductors (left) have their optical absorption edge at lower energy than the insulators (right). This is because energy band formation reduces the energy difference in the original two-level scheme, whereas

Vizio EX1018 Page 0074

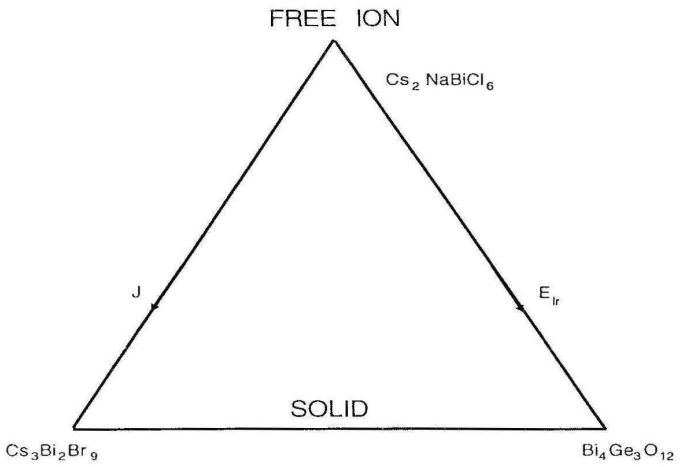

Fig. 3.26. Schematic representation of the transition from the free-ion state (apex) to the condensed-matter state (base). See also text. E_{lr} indicates the electron-lattice coupling, J the orbital overlap. Along the right-hand leg localisation increases, along the left-hand leg delocalisation. The examples concern the Bi^{3+} ion. In $Cs_2NaBiCl_6$ the spectra can be described by a small Huang-Rhys coupling parameter (S), in $Bi_4Ge_3O_{12}$ the value of S is very large, whereas $Cs_3Bi_2Br_9$ is a semiconductor

the parabola offset increases this difference: $CsVO_3$ has its optical absorption edge at $\sim$ 3.4 eV, and YVO_4 at $\sim$ 4 eV. Even more impressive are $Bi_{12}GeO_{20}$ ($\sim$ 3 eV) and $Bi_4Ge_3O_{12}$ ($\sim$ 5 eV).

Intermediary cases are $SrTiO_3$ and $KTiOPO_4$. Their emissions show small Stokes shifts compared to that of isolated titanate groups. This implies that only at liquid helium temperatures is luminescence observed. The excited state needs only a low thermal activation energy to become mobile.

Interestingly enough, $CsPbCl_3$ is a semiconductor, but $PbCl_2$ an insulator. This is related to the way in which the chloro-lead polyhedra are coupled in the crystal structure. In $CsPbCl_3$ this coupling favours energy band formation.

The triangle of Figure 3.26 has the advantage that it is possible to locate the different luminescent compounds in such a way that their luminescence properties are immediately characterized, albeit approximatively.

3.3.10 Cross-Luminescence

Recently there has been a lot of interest in the luminescence of BaF_2. Its crystals have a potential as a scintillator material (detection of gamma rays, see Chapter 9). They show a luminescence at 220 nm with a very short decay time, viz., 600 ps. This luminescence is of a new type (cross-luminescence). Its nature has been unraveled by Russian investigators [28]. Excitation with about 10 eV excites anion excitons i.e. excitons of which the hole is trapped on F^-. Upon recombination these anion excitons show an emission at about 4.1 eV (300 nm). This is an emission of the type

Vizio EX1018 Page 0075

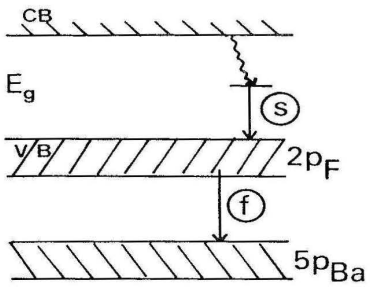

Fig. 3.27. Energy level scheme of BaF_2 showing cross luminescence (f). The exciton luminescence is indicated (s). See also text

observed for alkali halides (Sect. 3.3.1). Excitation with about 18 eV excites cation excitons. These do not recombine in a simple way, but by a so-called cross-transition: an electron jumps from the F^- ion ($2p$ orbital) into the hole in the $5p$ orbital of Ba^{2+} (see Figure 3.27). This is accompanied by emission at about 5.7 eV (220 nm), and weaker emissions at even higher energy. Since the energy difference between the $2p$ (F^-) and the $5p$ (Ba^{2+}) energy band is less than the band gap ($\sim$ 10 eV), the corresponding emission is observed as part of the intrinsic emission of BaF_2. The 200 nm emission shows practically no temperature quenching up to room temperature, whereas the 300 nm emission is for the greater part quenched under these conditions.

Other compounds for which this phenomenon has been found are CsCl and CsBr, and KF, $KMgF_3$, $KCaF_3$, and K_2YF_5.

3.4 Afterglow

Afterglow is the phenomenon that luminescence can still be observed a long time after the end of the excitation pulse. A long time here is defined as a time much longer than the decay time τ_R of the luminescence (Sect. 3.2). Everybody knows this phenomenon from the luminescent lamp that still glows after being switched off. For certain applications the level of afterglow should be negligbly low.

Afterglow is due to the phenomenon that radiant recombination of electrons and holes is sometimes considerably delayed due to trapping of electrons or holes. Figure 3.28 gives a simple illustration. A semiconductor contains, next to the luminescent centers, also centers which trap electrons. Excitation with energy above E_g yields free electrons and holes. Let us assume that the holes are trapped by the luminescent center, whereas the electrons in the conduction band recombine with the holes yielding emission.

However, part of the electrons are trapped in the electron trap center, from where they escape thermally after some time. Only then they recombine with a trapped hole. The corresponding emission occurs with considerable delay and is called afterglow.

Vizio EX1018 Page 0076

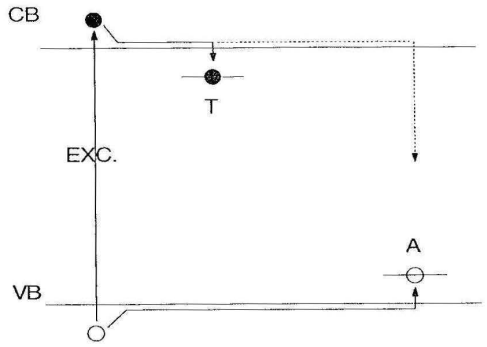

Fig. 3.28. The afterglow mechanism. Excitation (EXC) creates free electrons and holes. The holes are trapped at the level A where recombination with an electron yields radiative recombination (emission). However, the electron is trapped at the level T, so that it arrives only at A after considerable delay. Therefore afterglow results

A simple example is $Y_3Ga_5O_{12}:Cr^{3+}$. Holes are trapped by Cr^{3+}, forming Cr^{4+}. Electrons recombine with Cr^{4+}, yielding excited Cr^{3+} ions which emit. However, part of the electrons are trapped at oxygen vacancies from where they escape later to yield afterglow [29].

3.5 Thermoluminescence

If the system depicted in Figure 3.28 is irradiated with $E > E_g$ at temperatures which are too low to allow electrons to escape from the traps, the traps are filled and can only be emptied by increasing the temperature. If the temperature is now increased regularly, emission from the luminescent center will occur at temperatures where the traps are emptied thermally. The resulting curve of luminescence intensity versus temperature is called a glow curve. An example is given in Figure 3.29. From the position and shape of the glow peaks, information can be obtained about the traps [30]. Note that this is thermal stimulation of luminescence (and not thermal excitation, since the excitation has occurred before, viz. during filling of the traps).

It is also possible to perform optical stimulation, viz. by irradiation with light the energy of which is sufficient to excite the electron from the trap into the conduction band. In certain applications this photostimulation plays an important role (see Chapter 8).

Vizio EX1018 Page 0077

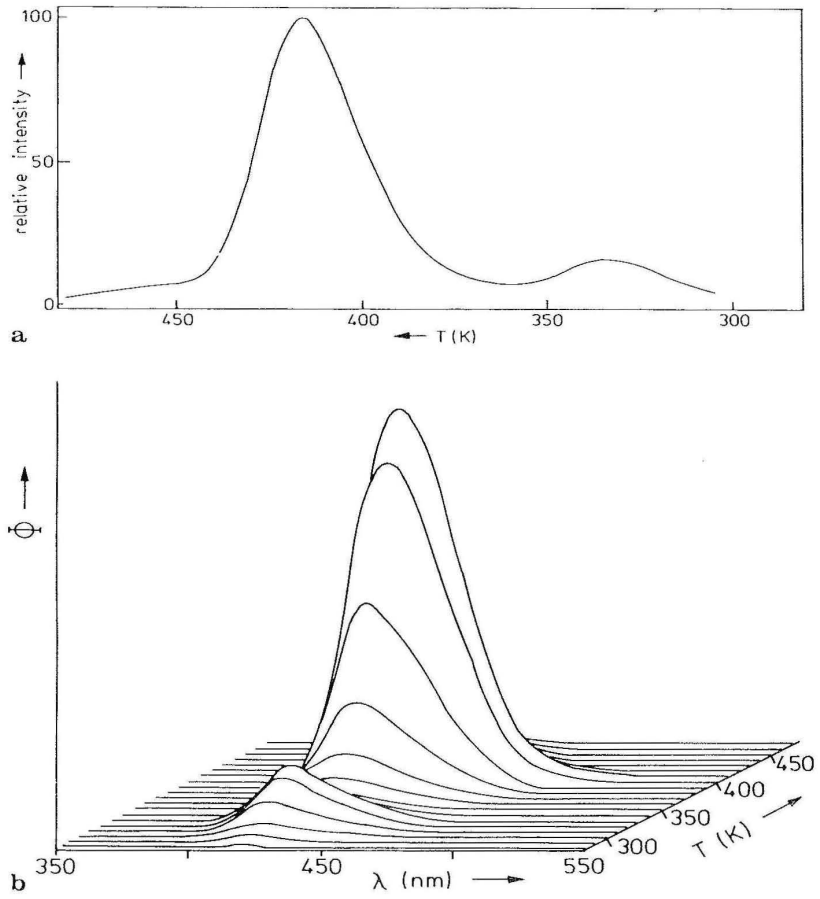

Fig. 3.29. Glow curve of X-ray irradiated $Ba_2B_5O_9Br:Eu^{2+}$ (*top*). The luminescence intensity is given as a function of temperature. The presence of two glow peaks indicates the presence of two traps with different trap depths in the host lattice. The lower picture presents the thermoluminescence emission spectra of the same sample. Actually the top curve is a cross section of the bottom picture. For reference, see figure 3.15.

3.6. Stimulated Emission

It should be realized that absorption and emission as discussed in Chapters 2 and 3 are different processes, since the former needs a radiation field and the latter not. Einstein considered the problem of transition rates in the presence of a radiation field [31]. For the transition rate from lower to upper level he wrote $w = B\rho$, where B is the Einstein coefficient of (stimulated) absorption and ρ is the radiation density.

The radiation field induces also a transition from the upper to the lower state (stimulated emission). The rate is $w' = B'\rho$, where B′ is the Einstein coefficient of stimulated emission. The rate of spontaneous emission is $w'' = A$, with A the coefficient of spontaneous emission (note the absence of ρ in this expression). This is

Vizio EX1018 Page 0078

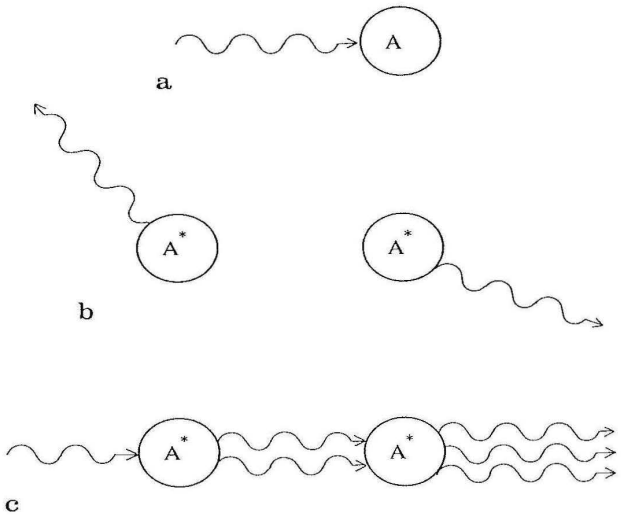

Fig. 3.30. Schematic representation of *a* absorption (A absorbs radiation and reaches the excited state A* which is not shown in *a*); *b* spontaneous emission from two species A* (the two emissions are not correlated); *c* stimulated emission (incoming radiation on the left-hand side "forces" two A* species to return to the ground state; the outcoming radiation on the right-hand side is amplified by a factor 3 as far as the amplitude is concerned)

shown schematically in Figure 3.30. It can be derived that $B' = B$ and $A = 8\pi h\nu^3 c^{-3} B$ (ν is the frequency of the emitted radiation, c is the speed of light).

If the two levels have an energy separation of, for example, 20 000 cm^{-1} (visible light), the lower level will be predominantly occupied, i.e. stimulated emission can be neglected. This justifies the approach of Chapters 2 and 3. In the case of three or more levels, the situation in which one of the higher levels has a higher occupation than the ground level (population inversion) can, under special conditions, be realized.

This can be illustrated on the Cr^{3+} ion in a strong crystal field. Its energy level scheme is given in Figure 3.31. Upon irradiation into the $^4A_2 \rightarrow {}^4T_2$ transition with high intensity, population inversion between the ^2E and $^4A_2$ levels can be obtained. This is due to the fact that the $^4T_2$ level empties rapidly into the ^2E level which in turn has a very long life time (ms) in view of the spin selection rule.

If one of the excited Cr^{3+} ions decays spontaneously, the emitted photon will stimulate other excited Cr^{3+} ions to decay by stimulated emission, so that there is an amplification of the original photon. This is the principle of laser action (laser stands for **l**ight **a**mplification by **s**timulated **e**mission of **r**adiation). The amplification ends when the population inversion is over, since absorption then dominates stimulated emission.

Therefore, a four-level laser offers an important advantage, viz. population inversion is easier to obtain and to maintain (see Figure 3.32): level 4 should decay rapidly to the ground level 1, so that any population of level 3 corresponds to population inversion. The Nd^{3+} ion serves in this way.

Vizio EX1018 Page 0079

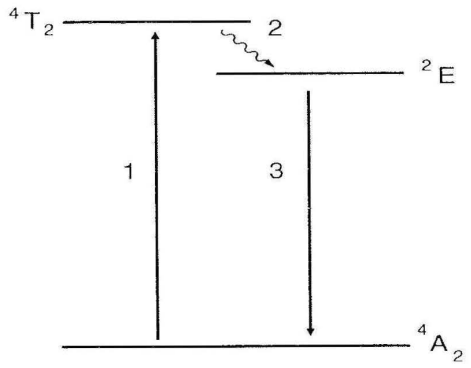

Fig. 3.31. The ruby three-level laser. The pumping transition is 1, the lasing transition 3. The nonradiative transition 2 is fast relative to the radiative inverse of 1. The level notations are for Cr^{3+}. The orders of magnitude of the relevant rates are $p(^4T_2 \rightarrow {}^4A_2) = 10^5\ s^{-1}$, $p(^4T_2 \rightarrow {}^2E) = 10^7\ s^{-1}$, $p(^2E \rightarrow {}^4A_2) = 10^2\ s^{-1}$

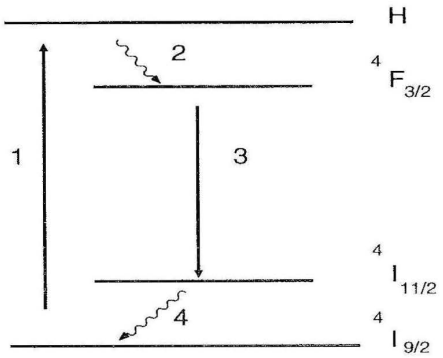

Fig. 3.32. The four-level laser scheme. Pumping transition is 1, lasing transition 3, nonradiative transitions 2 and 4. On the right-hand side the level notation for Nd^{3+} for the case of the 1064 nm laser action is given. H denotes levels above $^4F_{3/2}$; further $^4I_{11/2}$ cannot be thermally populated since it is about 2000 cm^{-1} above the ground state

This book does not intend to deal with laser physics and all the possible types of lasers. Two remarks are still worth noting:

- By using broad-band emission as depicted in Figure 3.1, it is possible to make a tunable laser. This is a four-level laser (level 1 is the lowest vibrational level of the ground state parabola, level 2 are the vibrational levels of the excited state reached after optical absorption, level 3 is the lowest vibrational level of the excited state parabola, and level 4 is one of the vibrational levels of the ground state parabola reached after emission). Tunability is achieved by selecting level 4.
- A laser material should satisfy several requirements. One of these is that it shows efficient luminescence. Further, laser materials should be characterized by careful spectroscopic measurements.

Vizio EX1018 Page 0080

In view of the latter remark the phenomenon of stimulated emission has been mentioned, and certain laser materials will be mentioned later in this book. History illustrates this by the fact that ruby, investigated long ago by Becquerel, is the material on which the first solid state laser was based. In this chapter the return from the excited state to the ground state was assumed to be radiative only. The next chapter considers nonradiative transitions.

References

1. Henderson B, Imbusch GF (1989) Optical spectroscopy of inorganic solids. Clarendon, Oxford
2. Donker H, Smit WMA, Blasse G (1989) J. Phys. Chem. Solids 50:603; Wernicke R, Kupka H, Ensslin W, Schmidtke HH (1980) Chem. Phys. 47:235
3. Wolfert A, Oomen EWJL, Blasse G (1985) J. Solid State Chem. 59:280
4. Atkins PW (1990) Physical chemistry, 4th ed. Oxford University Press, Oxford
5. Tanimura K, Makimura T, Shibata T, Itoh N, Tokizaki T, Iwai S, Nakamura A (1993) Proc. int. conf. defects insulating materials. S. Nordkirchen, World Scientific, Singapore, p 84; Puchin VE, Shluger AL, Tanimura K, Stok N (1993) Phys Rev B47:6226
6. Blasse G (1992) Int Rev Phys Chem 11:71
7. Brixner LH, Blasse G (1989) Chem. Phys. Letters 157:283
8. Judd BR (1962) Phys. Rev. 127:750; Ofelt GS (1962) J. Chem. Phys. 37:511
9. Mello Donega C de, Meijerink A, Blasse G (1992) J. Phys.: Cond. Matter 4:8889
10. Di Bartolo B (1968) Optical interactions in solids, Wiley, New York
11. Schotanus P, van Eijk CWE, Hollander RW (1988) Nucl. Instr. Methods A 272:913; Schotanus P, Dorenbos P, van Eijk CWE, Hollander RW (1989) Nucl. Instr. Methods A 284:531
12. Meijerink A, Nuyten J, Blasse G (1989) J. Luminescence 44:19
13. Blasse G, Dirksen GJ, Meijerink A (1990) Chem. Phys. Letters 167:41
14. Blasse G, de Korte PHM (1981) J. Inorg. Nucl. Chem. 43:1505
15. Herren M, Güdel HU, Albrecht C, Reinen D (1991) Chem. Phys. Letters 183:98
16. Blasse G (1980) Structure and Bonding 42:1
17. Barendswaard W, van der Waals JH (1986) Molec. Phys. 59:337; Barendswaard W, van Tol J, Weber RT, van der Waals JH (1989) Molec. Phys. 67:651
18. Hazenkamp MF, thesis, University Utrecht, 1992
19. Blasse G (1991) Structure and Bonding 76:153
20. Tol van J, van der Waals JH (1992) Chem. Phys. Letters 194:288
21. Bruin de TJM, Wiegel M, Dirksen GJ, Blasse G (1993) J. Solid State Chem. 107:397
22. Ranfagni A, Mugni M, Bacci M, Viliani G, Fontana MP (1983) Adv. Physics 32:823
23. Blasse G (1988) Progress Solid State Chem. 18:79
24. Bersuker IB, Polinger VZ (1989) Vibronic interactions in molecules and crystals, Springer, Berlin
25. Blasse G, Topics in Current Chemistry, in press.
26. Denning RG (1992) Structure and Bonding 79:215
27. Kitai AH (ed) Solid state luminescence. Theory Materials and Devices, Chapman and Hall, 1993
28. Valbis YaA, Rachko ZA, Yansons YaL (1985) JETP Letters 42:172; Aleksandrov YuM, Makhov VN, Rodnyl PA, Syreinshchikova TI, Yakimenko MN (1984) Sov. Phys. Solid State 26: 1734
29. Grabmaier BC (1993) Proc. int. conf. defects insulating materials, Nordkirchen, World Scientific, Singapore, p 350; Blasse G, Grabmaier BC, Ostertag M (1993) J. Alloys Compounds 200: 17
30. McKeever SWS (1985) Thermoluminescence of solids, Cambridge University, Cambridge
31. For a simple account, see ref. [4]. For a more detailed account ref. [1]

Vizio EX1018 Page 0081

CHAPTER 4

Nonradiative Transitions

4.1 Introduction

Radiative return from the excited state to the ground state (Chapter 3) is not the only possibility of completing the cycle. The alternative is nonradiative return, i.e. a return without emission of radiation. Nonradiative processes will always compete with radiative processes. Since one of the most important requirements for a luminescent material is a high light output, it is imperative that in such a material the radiative processes have a much higher probability than the nonradiative ones.

All energy absorbed by the material which is not emitted as radiation (luminescence) is dissipated to the crystal lattice (radiationless processes). It is, therefore, imperative to suppress those radiationless processes which compete with the emission process. There are, however, also nonradiative processes which favour a high light output, viz. those which ensure a more effective feeding of the luminescent activator and/or population of the emitting level.

Table 4.1 gives the quantum efficiencies (see Sect. 4.3) of some important photoluminescent materials. Note that the maximum obtainable value of 100% is not obtained by far. The complicated composition $NaGdF_4$–Ce,Tb gives the nearest approach to this value. As we will see below, this is due to the fact that the radiationless feeding-processes of the emitting Tb^{3+} ion are, although complicated, very effective, and the radiationless processes competing with the emission very ineffective. In $CaWO_4$, on the other hand, the emitting tungstate group is excited directly, and the 70% quantum efficiency is due to a ratio of the radiative and nonradiative decay rates of the emitting level of about 2:1.

Table 4.1. Quantum efficiencies q of some photoluminescent materials under ultraviolet excitation at room temperature

Material	q(%)
Zn_2SiO_4–Mn^{2+}	70
YVO_4–Eu^{3+}	70
$CaWO_4$	70
$Ca_5(PO_4)_3(F,Cl)$–Sb^{3+},Mn^{2+}	71
$NaGdF_4$–Ce^{3+}, Tb^{3+}	95

Vizio EX1018 Page 0082

These observations illustrate that it is important to have a good understanding of radiationless processes in order to understand, to improve, and to predict luminescent materials. There are several approaches to this difficult problem [1,2]. In our opinion all of these are useful. One of these is a completely theoretical approach. This may nowadays be of great use in understanding specific, simple situations. However, it cannot be used with much success to account for the properties of a large number of different materials.

There are also general, approximative methods for studying nonradiative processes. A good example is the book by Struck and Fonger [3]. Our approach is probably the simplest one. The main characteristic is that the physical parameters are kept as simple as possible, whereas the chemical parameters are widely varied, i.e. by studying a large number of different materials we try to find out in how far the simple physical model is still able to account for the results. The great advantages of this method are its simplicity and predictive ability.

This chapter is organized as follows. In Sect. 4.2 we consider one isolated luminescent center and the possible nonradiative transitions in such a center. In Sect. 4.3 we define the several ways to express the efficiency of a luminescent material. In Sect. 4.4 we discuss the conversion efficiency of a luminescent material upon host lattice excitation over the energy band gap E_g. Finally Sections 4.5 and 4.6 show some other possiblities for nonradiative transitions.

4.2 Nonradiative Transitions in an Isolated Luminescent Centre

In Chapter 3 it was assumed that the return from the excited state to the ground state is radiative. This is usually not the case. Actually there are many centers which do not luminesce at all. Let us consider the configurational coordinate diagrams of Figure 4.1 in order to understand the relevant physical processes. Figure 4.1a presents essentially the same as Figure 3.1. Absorption and emission transitions are possible and Stokes shifted relative to each other. The relaxed-excited-state may, however, reach the crossing of the two parabolas if the temperature is high enough. Via the crossing it is possible to return to the ground state in a nonradiative manner (see arrow in Figure 4.1a). The excitation energy is then completely given up as heat to the lattice. This model accounts for the thermal quenching of luminescence (the latter being essentially a low-temperature phenomenon). The transition from parabola e to parabola g will not be considered further here. Essentially it is a transition between two (nearly) resonant vibrational levels, one belonging to e, the other to g. It will be clear that the larger the offset between the parabolas, the easier the transition occurs.

In Figure 4.1b, the parabolas are parallel ($S = 0$) and will never cross. It is impossible to reach the ground state in the way described for Figure 4.1a. However, also here nonradiative return to the ground state is possible if certain conditions are fulfilled, viz. the energy difference ΔE is equal to or less than 4–5 times the higher

Vizio EX1018 Page 0083

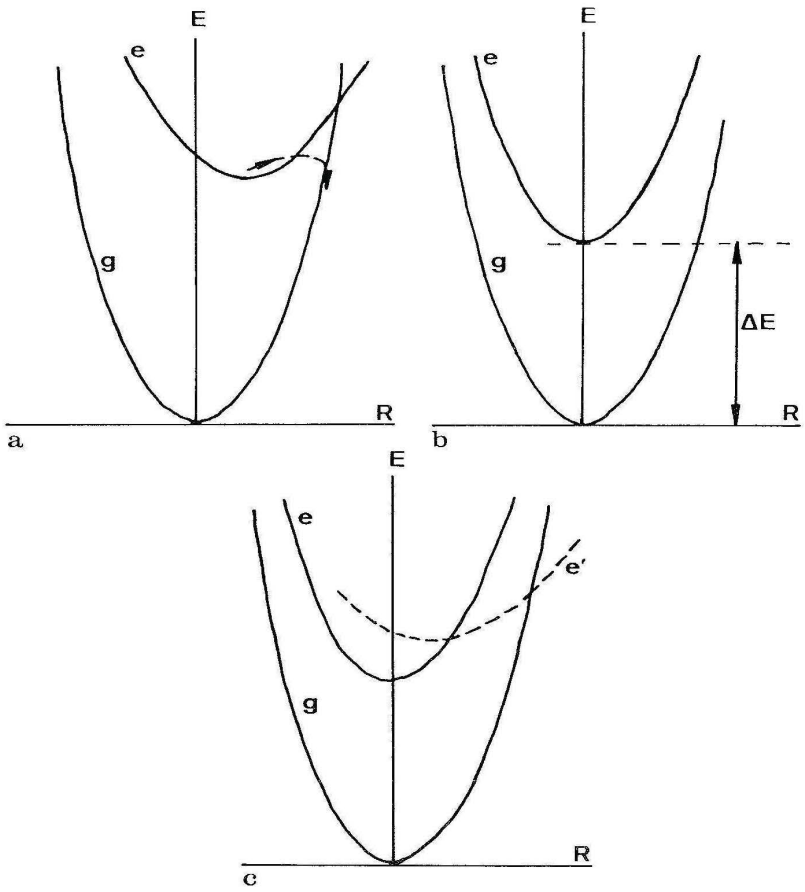

Fig. 4.1. Configurational coordinate diagrams illustrating nonradiative transitions. The ground state parabola is indicated by g, the excited state parabolas by e and e′. See also text. In (*a*), the arrow indicates a nonradiative transition from e to g, which quenches the luminescence at higher temperatures. In (*b*), ΔE is the energy difference between e and g. In (*c*), excitation is into e′; this level feeds the emitting level e

vibrational frequency of the surroundings. In that case, this amount of energy can simultaneously excite a few high-energy vibrations, and is then lost for the radiative process. Usually this nonradiative process is called multi-phonon emission.

In Figure 4.1c both processes are possible in a three-parabolas-diagram. The parallel parabolas will belong to the same configuration, so that they are connected by forbidden optical transitions only. The third one originates from a different configuration and is probably connected to the ground state by an allowed transition. This situation occurs often. Excitation (absorption) occurs now from the ground state to the highest parabola in the allowed transition. From here the system relaxes to the relaxed excited state of the second parabola. Figure 4.1c shows that the nonradiative transition between the two upper parabolas is easy. Emission occurs now from the

Vizio EX1018 Page 0084

second parabola (line emission). This situation is found for $Al_2O_3:Cr^{3+}$ ($^4A_2 \rightarrow {}^4T_2$ excitation, $^4T_2 \rightarrow {}^2E$ relaxation, $^2E \rightarrow {}^4A_2$ emission), Eu^{3+} ($^7F \rightarrow$ charge-transfer-state excitation, charge-transfer-state to ^5D relaxation, $^5D \rightarrow {}^7F$ emission), and Tb^{3+} ($^7F \rightarrow 4f^75d$ excitation, $4f^75d \rightarrow {}^5D$ relaxation, $^5D \rightarrow {}^7F$ emission).

In general the temperature dependence of the nonradiative processes is reasonably well understood. However, the magnitude of the nonradiative rate is not, and can also not be calculated with any accuracy except for the weak-coupling case. The reason for this is that the temperature dependence stems from the phonon statistics which is known. However, the physical processes are not accurately known. Especially the deviation from parabolic behaviour in the configurational coordinate diagram (anharmonicity) may influence the nonradiative rate with many powers of ten. However, it will be clear that the offset between the two parabolas (ΔR) is a very important parameter for the nonradiative transition rate. This rate will increase dramatically if ΔR becomes larger.

We consider first the weak-coupling case ($S \sim 0$), and subsequently the intermediate- and strong-coupling cases ($S \gg 0$).

4.2.1 The Weak-Coupling Case

Nonradiative transitions in the weak-coupling approximation are probably the best understood nonradiative processes. The experimental data relate mainly to the rare-earth ions, as far as their sharp-line transitions are considered (i.e. intra-$4f^n$-configuration transitions). The topic has been discussed in books and review papers [1,2,4,5]. We summarize as follows:

For transitions between levels of a $4f^n$ configuration the temperature dependence of the nonradiative rate is given by

$$W(T) = W(0)(n+1)^p \tag{4.1}$$

where W(T) is the rate at temperature T, $p = \frac{\Delta E}{h\nu}$, ΔE the energy difference between the levels involved, and

$$n = [\exp(\frac{h\nu}{kT}) - 1]^{-1}. \tag{4.2}$$

W(0) is large for low p, i.e. for small ΔE or high vibrational frequencies. Further

$$W(0) = \beta \exp[-(\Delta E - 2h\nu_{max})\alpha], \tag{4.3}$$

with α and β constants, and ν_{max} the highest available vibrational frequency of the surroundings of the rare earth ion. This is the energy-gap law in the revised form by Van Dijk and Schuurmans [6], which makes it possible to calculate W with an accuracy of one order of magnitude.

Let us illustrate this with some consequences. In aqueous solutions or in hydrates the rare earth ions do not emit efficiently with the exception of Gd^{3+} ($\Delta E = 32\,000$ cm^{-1}, $\nu_{max} \simeq 3500$ cm^{-1}). For Tb^{3+} ($\Delta E \simeq 15|000$ cm^{-1}), and especially

Vizio EX1018 Page 0085

Eu^{3+} ($\Delta E \simeq 12|000\ cm^{-1}$), the quantum efficiencies (q) are depressed, and the other rare earth ions do practically not emit at all. For solids this can be nicely studied in the host lattice $NaLa(SO_4)_2.H_2O$ where the rare earth site is coordinated to one H_2O molecule only. The q values are as follows: Gd^{3+} q = 100%, Tb^{3+} 70%, Eu^{3+} 10%, $Sm^{3+} \sim 1\%$, $Dy^{3+} \sim 1\%$.

In the classic oxide glasses the rare-earth ions do not emit efficiently, since $\nu_{max} \simeq 1000$–$1200\ cm^{-1}$ (silicates, borates, phosphates). Only Gd^{3+}, Tb^{3+} and Eu^{3+} show efficient luminescence. This situation changes drastically by using fluoride or chalcogenide glasses, where ν_{max} is considerably lower. A very interesting lattice in this connection is $Eu_2Mg_3(NO_3)_{12}\cdot 24H_2O$. At first sight the large number of water molecules is expected to quench the Eu^{3+} emission completely. However, the Eu^{3+} ions are bidentately coordinated by six nitrate ions which shield them from the water molecules. The quantum efficiency is high.

Ions like Eu^{3+} and Tb^{3+} may emit from higher excited states: Eu^{3+} not only from $^5D_0$ (red), but also from $^5D_1$ (green) and $^5D_2$ (blue). However, this depends critically upon the host lattice. In Y_2O_3–Eu^{3+}, for example, all these emissions are observed, since $\nu_{max} \simeq 600\ cm^{-1}$. In borates and silicates, however, they are not.

This can be well studied by laser spectroscopy. An example is $NaGdTiO_4:Eu^{3+}$ [7]. The time dependence of the Eu^{3+} emission in $NaGdTiO_4$ upon excitation into the $^5D_1$ level of Eu^{3+} is as follows: 10 μs after the excitation pulse the emission originates mainly from the $^5D_1$ level, but after longer times the $^5D_1$ intensity has decreased and that of $^5D_0$ increased (see Figure 4.2). The decay curves of the $^5D_0$ emission show a build-up. From these data the rate for $^5D_1 \rightarrow {}^5D_0$ decay is found to be $1.3 \times 10^4 s^{-1}$ at 4.2 K. Its temperature dependence is given by $(n + 1)^p$ as argued above. The value of p turns out to be 5, the vibrational frequency involved being $347\ cm^{-1}$. This corresponds to the Eu–O stretching vibration. At 300 K this nonradiative rate is about $4 \times 10^4 s^{-1}$. The values of the nonradiative rate exceed that of the radiative $^5D_1$–^7F_J rate ($\sim 10^3 s^{-1}$), so that the nonradiative process dominates and the emission occurs mainly from the $^5D_0$ level. In compounds with higher phonon frequencies available (e.g. borates, silicates), the $^5D_1$ emission of Eu^{3+} is usually hardly detectable, since the value of p is then much lower.

The Tb^{3+} ion may not only emit from $^5D_4$ (green), but also from $^5D_3$ (blue). ΔE is about $5000\ cm^{-1}$, much larger than in the case of Eu^{3+}. Diluted Tb^{3+} systems show, therefore, always some blue Tb^{3+} emission, unless ν_{max} is very high. Please note that in these examples we consider only ions interacting with their immediate surroundings and not with other luminescent ions. In Chapter 5 the quenching of higher level emission due to interaction with another centre of the same kind will be discussed (cross relaxation).

Finally we pay attention to Gd^{3+} ($4f^7$). Its energy level scheme is given in Figure 4.3. The excited levels are in the ultraviolet and the corresponding transitions have low oscillator strengths. As a consequence, accurate spectroscopy can only be performed with ultraviolet tunable lasers and/or X-ray excitation.

The emission transition $^6P_J \rightarrow {}^8S$ occurs over an energy gap which is about $32\,000\ cm^{-1}$. Nonradiative transitions cannot compete with this radiative one, because it occurs over such a large ΔE. Even water molecules ($\nu \sim 3500\ cm^{-1}$) are not able

Vizio EX1018 Page 0086

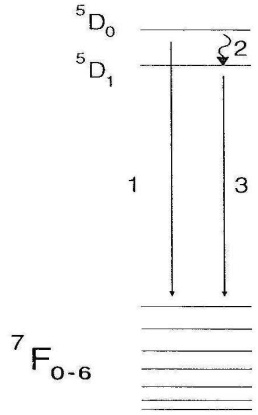

Fig. 4.2. Energy level scheme of Eu^{3+}. The $^5D_1$ level can decay radiatively to the ^7F_J levels (arrow 1), or nonradiatively to the $^5D_0$ level (arrow 2). The latter decay is followed by $^5D_0 \rightarrow {}^7F_J$ emission (arrow 3). The amount of $^5D_1$ emission is determined by the rate ratio of processes 1 and 2

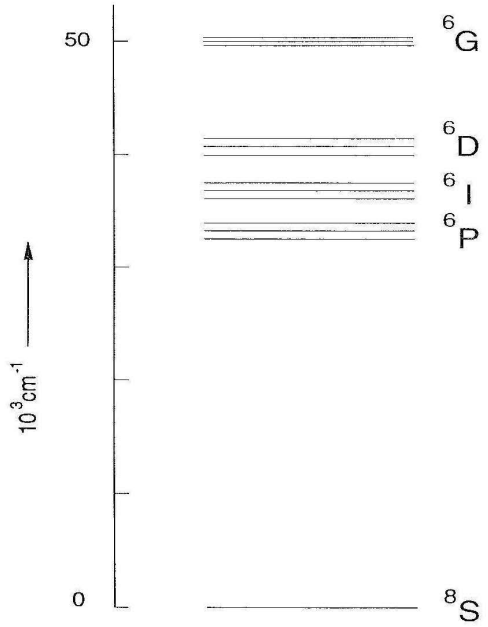

Fig. 4.3. Energy level scheme of the Gd^{3+} ion

to quench the Gd^{3+} emission. The emission can only be quenched by transfer to other luminescent centres (see Chapter 5).

In some host lattices emission has also been observed from the higher excited levels ^6I_J, ^6D_J, and even ^6G_J. However, this depends strongly on the host lattice. If

Vizio EX1018 Page 0087

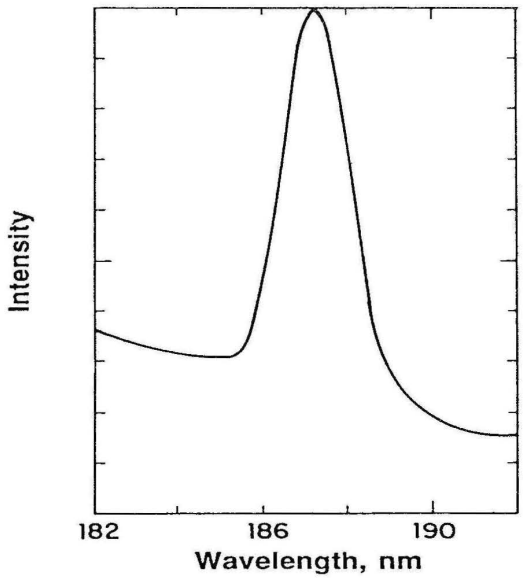

Fig. 4.4. The 187 nm emission line of Gd^{3+} (in Y_2O_3). Excitation is by X rays

the maximum vibrational frequency is low, and the host lattice transparant, emission can be observed from all these levels, up to the ^6G_J level (at about 205 nm) (see Fig. 3.9). There is even evidence for a higher level with $\sim$ 185 nm emission. Figure 4.4 gives an example. In the case of borates and hydrates, however, all these emissions are quenched in favour of the ^6P_J emission. This is a clear demonstration that higher-frequency vibrations promote the radiationless transitions to the ^6P_J levels.

4.2.2 The Intermediate- and Strong-Coupling Cases

This section starts by illustrating how important the value of the parabola offset (ΔR) is for the nonradiative transition rate. We will use several examples. First we will consider $CaWO_4$, a well-known X-ray phosphor for more than seventy-five years. The luminescent group is the tungstate group, a distinct example of a center for which the strong-coupling scheme holds (see Chapters 2 and 3). $CaWO_4$ is a very efficient luminescent material at room temperature. The isomorphous $SrWO_4$, however, does not emit at that temperature, but has to be cooled down in order to reach a reasonably efficient luminescence. Also $BaWO_4$ has the same crystal structure, but even at 4.2 K it does not emit with high efficiency. Nevertheless the ground state properties of the tungstate group in these compounds (distances, vibrational frequencies) are practically equal. The strongly different radiationless processes have to be ascribed to a difference in ΔR, i.e. the parabola offset. Since the ionic radii of Ca^{2+}, Sr^{2+}, Ba^{2+} increase in that order, it seems obvious to assume that this is the reason why the offset increases, i.e. why the rate of the radiationless processes increases, as observed experimentally. The softer the surroundings, the larger is ΔR. Here it is assumed that the presence of ions

Vizio EX1018 Page 0088

Table 4.2. Thermal quenching of the uranate luminescence of ordered perovskites A_2BWO_6–U^{6+}. Compare also Figure 4.5. Data from Ref. [8]

A_2BWO_6–U		T_q(K)[1]	ΔR(a.u.)[2]
A=Ba	B=Ba	180	10.9
Ba	Sr	240	10.6
Ba	Ca	310	10.2
Ba	Mg	350	10.0
Sr	Mg	350	10.0
Ca	Mg	350	10.0

1. Quenching temperature of the uranate luminescence.
2. ΔR in arbitrary units, calculated by the Struck and Fonger method [3]. ΔR is arbitrarily put at 10.0 for Ba_2MgWO_6.

with a large radius around the luminescent center is equivalent to soft surroundings. This seems a reasonable assumption.

There is a more impressive experiment to prove this simple model, viz. the luminescence in the ordered perovskites A_2BWO_6 where A and B are alkaline earth ions. Table 4.2 presents the quenching temperatures of the luminescence of the UO_6 group in these lattices [8]. Those for the WO_6 group run parallel. These temperatures are used as a measure of the radiationless processes. The table shows that the radiationless rate does not depend on the nature of the ion A, whereas that of the ion B determines the value of this rate: the smaller the B ion, the higher the quenching temperature.

Figure 4.5 shows that an expansion of the luminescent UO_6 (or WO_6) octahedron (i.e. the parabola offset) is not directly counteracted by the A ion. However, the B ions are immediately involved, the angle U(W)–O–B being 180°. Table 4.2 also shows relative values of ΔR calculated from the Struck and Fonger model [3]. These scale indeed according to prediction. Note that the total change in ΔR is less than 10%. Since ΔR is less than 0.1 Å for the uranate group, the variation in ΔR in this series of compounds is less than 0.01 Å. This shows that small changes in ΔR result in drastic changes in the nonradiative rates.

It is well known that luminescent materials with high quantum efficiencies and quenching temperatures usually have stiff lattices, so that expansion upon excitation is counteracted, i.e. ΔR is as small as possible.

Table 4.3 shows for a series of borates how the Stokes shift, i.e. ΔR, increases if the size of the host lattice cation increases [9]. In $ScBO_3$ the rare earth ions are strongly compressed and the surroundings are stiff. Small Stokes shifts result for Ce^{3+}, Pr^{3+} and Bi^{3+}, but not for the much smaller Sb^{3+}. Note also, that the Stokes shift of the $4f$–$5d$transitions is less sensitive to the surroundings than that of the $5s$–$5p$ transitions.

Part of solid state chemistry is nowadays involved with what is called soft chemistry or soft materials. As a matter of fact these are not expected to luminesce, at least not when the luminescent centers are broad-band emitters. This has been shown to be the case, for example, for the isomorphous $Al_2(WO_4)_3$, $Sc_2(WO_4)_3$ and $Zr_2(PO_4)_2SO_4$. The Stokes shift of the tungstate and zirconate luminescence in these materials is enor-

Vizio EX1018 Page 0089

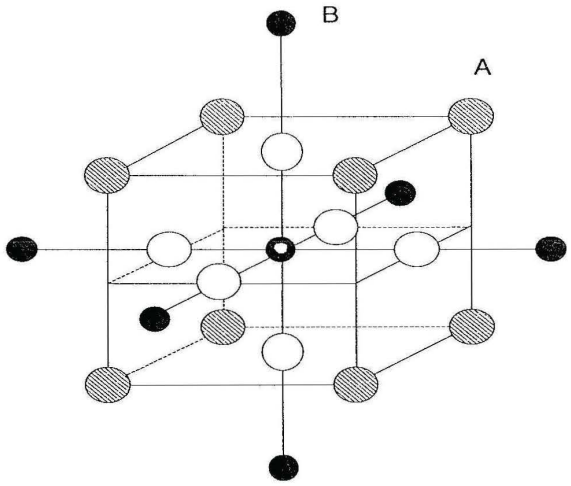

Fig. 4.5. The surroundings of the luminescent UO_6 or WO_6 group in the ordered perovskites A_2BWO_6. The luminescent center consists of the central black, white-centered ion and the six open ions (oxygen). This center is surrounded by a cube of hatched A ions and an octahedron of black B ions

Table 4.3. Stokes shift (10^3 cm^{-1}) of the band emission of some trivalent ions in the orthoborates MBO_3 (M=Sc,Y,La) After Ref. [9]

	$ScBO_3$	YBO_3*	$LaBO_3$
$Ce^{3+}(4f^1)$	1.2	2.0	2.4
$Pr^{3+}(4f^2)$	1.5	1.8	3.0
$Sb^{3+}(5s^2)$	7.9	$\binom{14.5}{16.0}$	19.5
$Bi^{3+}(6s^2)$	1.8	$\binom{5.1}{7.7}$	9.3

* This lattice contains two sites for Y.

mous, viz. some 20000 cm^{-1}. The quantum efficiencies, even at 4.2 K are low. This is all due to a large value of ΔR due to the soft surroundings of the luminescent centre.

This model in which the nonradiative transitions can be suppressed by stiff surroundings, can be most elegantly tested by studying the luminescence of rare-earth cryptates [10].

The cryptand ligands are organic cages. They were synthesized for the first time by Lehn who obtained the Nobel prize for Chemistry in 1987 for this achievement (together with Cram and Pederson). Figure 4.6 gives two examples. The 2.2.1 cryptand is just large enough to contain the Ce^{3+} ion, i.e. upon excitation the Ce^{3+} ion has not much space to expand. In fact the $[Ce \subset 2.2.1]^{3+}$ cryptate shows an efficient (broad-band) emission at room temperature with a small Stokes shift, in the solid state as well as in aqueous solution. The $[Ce \subset 2.2.2]^{3+}$ cryptate luminescence has a much larger Stokes shift. As a matter of fact the 2.2.2 cryptand offers a larger hole than the 2.2.1 cryptand.

Vizio EX1018 Page 0090

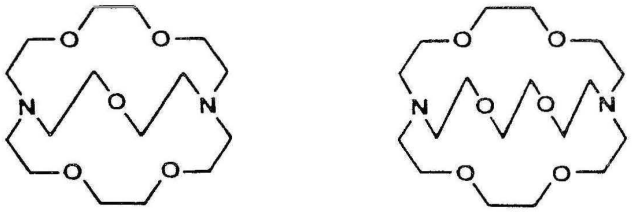

Fig. 4.6. The [2.2.1] and the [2.2.2] cryptands. The empty corners contain a–CH_2 group. These molecules have the shape of a cage in which a trivalent rare earth ion can be introduced

Table 4.4. The Stokes shift of the Ce^{3+} emission for several luminescent compositions/species

Composition/species	Stokes shift (cm^{-1})
$[Ce^{3+} \subset 2.2.1]$	2100
$[Ce^{3+} \subset 2.2.2]$	4000
Ce^{3+} in aqueous solution	5000
$Y_3Al_5O_{12}$–Ce^{3+}	3800
Y_2SiO_5–Ce^{3+}	2500
$ScBO_3$–Ce^{3+}	1200

Table 4.4 shows the Stokes shift of the Ce^{3+} emission in several surroundings. In the 2.2.1 cryptand the Ce^{3+} Stokes shift is smaller than in some commercial Ce^{3+}-activated phosphors (Y_2SiO_5–Ce, Ca_2AlSiO_7–Ce). It becomes very small in $ScBO_3$ (see above) and in CaF_2 and $CaSO_4$ where the Ce^{3+} ion carries an effectively positive charge which will make the Ca site smaller than it is on basis of the Ca^{2+} ionic radius.

The experiments treated above give ample evidence that ΔR should be as small as possible if an efficient luminescent material is required. Not only the value of ΔR is of importance. This can be shown by a simple model calculation [11]. We consider a luminescent material in which the luminescent centre is described with a single-configurational coordinate diagram with two parabolas with equal force constants k. The offset is ΔR, the vibrational frequency $h\nu$, and the energy difference between the parabolas E_{zp}. By introducing certain values for other parameters involved and following the Struck and Fonger approach [3], the temperature dependence of the luminescence efficiency can be calculated (see Fig. 4.7).

Note that the larger ΔR, the lower the quenching temperature of the luminescence, i.e. the more important the radiationless processes. High values of $h\nu$ also promote radiationless decay. For $h\nu = 600\ cm^{-1}$ the low-temperature value of the efficiency remains far below the maximum possible value, i.e. even at 0K the rate of the nonradiative processes is about equal to that of the radiative ones. This is due to tunnelling from the excited state parabola to the ground state parabola (Fig. 4.8). A decreasing value of E_{zp} also yields a lower quenching temperature.

Vizio EX1018 Page 0091

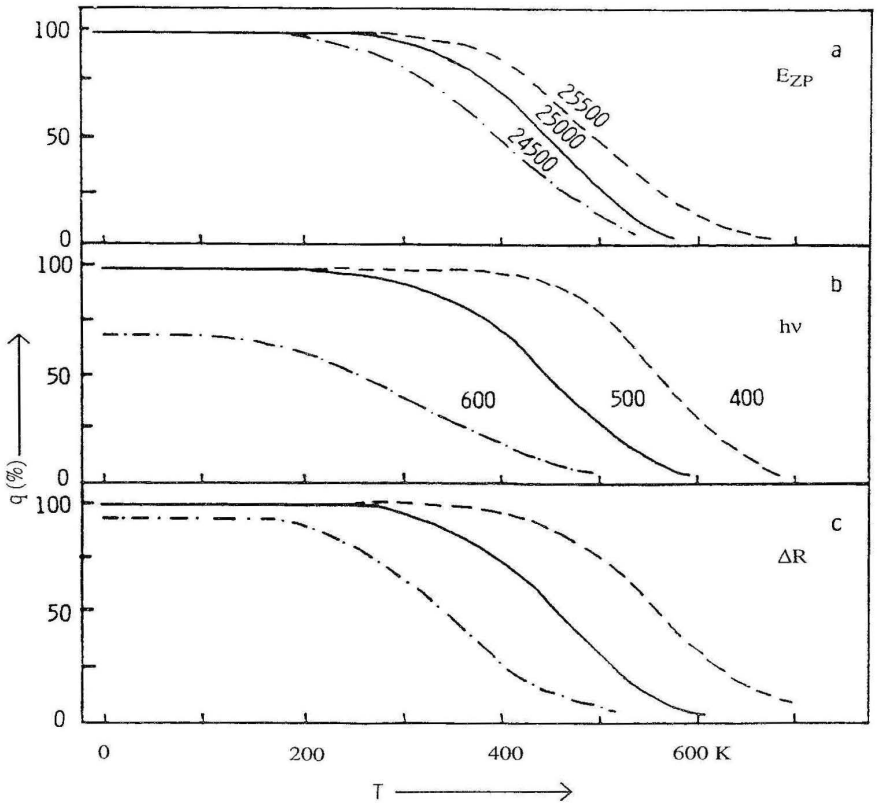

Fig. 4.7. Temperature dependence of the luminescence quantum efficiency (q) according to calculations on a model phosphor system. In (*a*) the energy difference between the parabola minima (E_{zp}) is varied (values in cm^{-1}). In (*b*) the vibrational frequency is varied (values in cm^{-1}). In (*c*) the parabola offset (ΔR) varies; it decreases from left to right by 6%

The latter is experimentally confirmed by a comparison of $CaWO_4$ and $CaMoO_4$. These compounds are comparable in many aspects. A striking difference is that the energy levels of the tungstate group lie some 5000 cm^{-1} higher than those of the molybdate group. For the room-temperature luminescence of these compounds such a difference has an important consequence: whereas $CaWO_4$ shows an efficient blue emission, the greenish emission of $CaMoO_4$ is partly quenched. This observation can be generalized: broad band emission is the more efficient, the shorter the maximum wavelengths of the excitation and emission bands are.

Let us now consider luminescent centers with three-parabola diagrams (Fig. 4.1.c). A clear example is the charge-transfer excitation of the Eu^{3+} luminescence, a process which is of large importance for applications. Consider the red phosphor in the three-color luminescent lamps. Its composition is $Y_2O_3:Eu$. Excitation at 254 nm in the charge- transfer state is followed by efficient red emission ($^5D_0$–$^7F_2$) within the $_4f^6$ configuration. Figure 4.9 shows the relevant configurational coordinate diagram.

Vizio EX1018 Page 0092

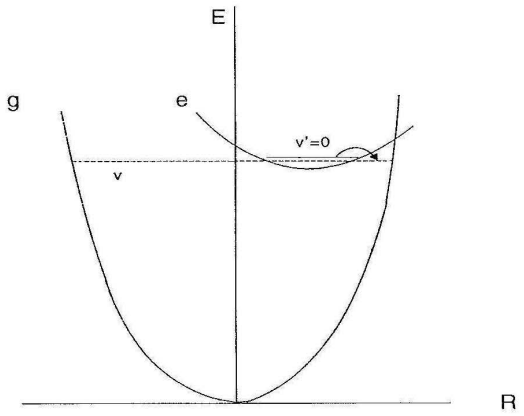

Fig. 4.8. The system can tunnel (arrow) from the lowest vibrational level $v' = 0$ of the excited state e to a high vibrational level $v = v$ of the ground state g. The v level is (nearly) resonant with the $v' = 0$ level. The tunnelling rate depends on the vibrational wave function overlap of the two vibrational levels. Since the wave function of v has its highest amplitude at the turning points (see Fig. 2.4), the tunnelling rate is at a maximum if the minimum of the e parabola reaches the turning point, i.e. if ΔR is large

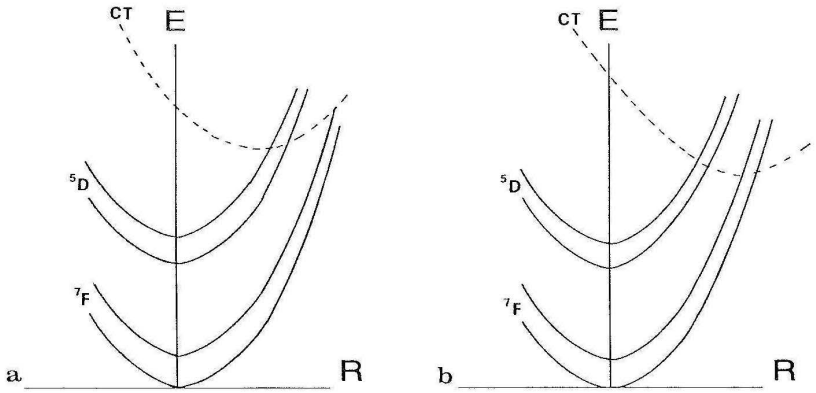

Fig. 4.9. The role of the charge-transfer state (CT) in the quenching of the luminescence of the Eu^{3+} ion. Only a few parabolas of the $_4f^6$ configuration have been drawn. In (*a*), the situation for $Y_2O_3:Eu^{3+}$ is depicted: the CT state feeds the emitting ^5D levels. In (*b*), the CT state has a larger offset. As a consequence the CT state populates, at least partly, the ground state levels, so that the luminescence is strongly reduced

Note that the useful properties of Y_2O_3–Eu^{3+} are based on a fast radiationless process, viz. the transition from the charge-transfer state to the excited levels of the $4f^6$ configuration. For crystalline GdB_3O_6–Eu^{3+} the same model holds. This composition

Vizio EX1018 Page 0093

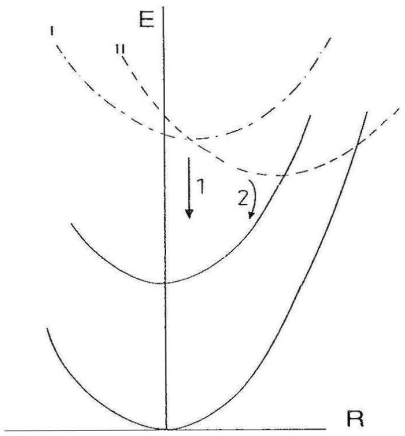

Fig. 4.10. Schematic configurational coordinate diagram for Pr^{3+} ($4f^2$). Drawn parabolas relate to the $4f^2$ configuration; the broken parabolas indicate two possible situations for the $4f^{5d}$ configuration (I and II). Excitation into I yields $d\rightarrow f$ emission from I (arrow 1). Excitation into II (with larger offset) yields a nonradiative transition to the $4f^2$ configuration (arrow 2) which may be followed by intraconfigurational $4f^2$ emission

can also be obtained as a glass. Interestingly enough, charge-transfer excitation in the glass results in Eu^{3+} luminescence with an efficiency which is an order of magnitude smaller than in the crystalline modification. This is also the case at 4.2 K. This observation has been ascribed to a larger offset of the charge-transfer parabola in the glass than in the crystal, so that in the glass the charge-transfer state empties mainly into the ^7F ground-state manifold. It is quite conceivable that the glass surroundings can counteract the expansion upon excitation less than the crystalline surroundings. The important consequence of this is that broad-band emission in glasses will have low efficiencies, unless the Stokes shift is small.

If the charge-transfer state moves to lower energy, the efficiency of the luminescence upon charge-transfer excitation decreases also. This is due to an increasing probability of the nonradiative transition from the charge-transfer state to the ^7F levels (compare the discussion on the difference between $CaWO_4$ and $CaMoO_4$ in this paragraph).

A different, but comparable, example is the Pr^{3+} ($4f2$) ion. There is an excited $4f5d$ configuration. Figure 4.10 gives the configurational coordinate diagram of Pr^{3+} in two different host lattices. If the offset of the $4f^{5d}$ state is small, radiative return to the $4f^2$ configuration has a higher probability than the nonradiative transition to the $4f^2$ configuration. If the offset is large, $4f^{5d}$ excitation leads to emission from the $4f^2$ configuration after a nonradiative $4f^5d \rightarrow 4f^2$ transition. The former situation is encountered for YBO_3, YOCl and LaB_3O_6, the latter for the apatite $Gd_{9.33}(SiO_4)_6O_2$ and Gd_2O_2S.

The Pr^{3+} case has an advantage over that of Eu^{3+}, viz. the higher excited state can emit, so that the Stokes shift can be measured. This gives information on the

Vizio EX1018 Page 0094

relaxation and the parabola offset. It was found that the nonradiative $4f^{5d} \rightarrow {}_4f^2$ transition becomes important if the Stokes shift is larger than 3000 cm^{-1}.

In conclusion, this section has summarized evidence in order to obtain some idea what are the factors determining the rate of radiationless processes in an isolated luminescent center, without going into any physical or mathematical details.

4.3 Efficiency

In the preceding section the expression "efficiency of the luminescence" was used frequently without giving a definition. A luminescent material which emits brilliantly is, of course, efficient. In this paragraph the several definitions of the efficiency of a luminescent material are given.

In the case of photoluminescence we distinguish the quantum efficiency (q), the radiant efficiency (η) and the luminous efficiency (L). The quantum efficiency q is defined as the ratio of the number of emitted quanta to the number of absorbed quanta. In the absence of competing radiationless transitions its value is 1 (or 100%). In the fundamental literature this is the important efficiency. The other two have a more technical importance.

The radiant efficiency η is defined as the ratio of the emitted luminescent power and the power absorbed by the material from the exciting radiation. The luminous efficiency L is the ratio of the luminous flux emitted by the material and the absorbed power.

Sometimes the term light output is used. This is the quantum efficiency multiplied by the amount of absorbed radiation. A high q does not necessarily imply a high light output: a photoluminescent material has only a high light output if the quantum efficiency and the optical absorption coeffient for the exciting wavelength are both high.

For cathode-ray (CR) excitation q is irrelevant. The radiant efficiency is defined as the ratio of the emitted power to the power of the electron beam falling on the luminescent material. This means that η_{CR} refers to the total power incident on the material, whereas η_{UV} refers to the power absorbed. The luminous efficiency for CR excitation is defined in a similar way as for photoexcitation. The radiant efficiency for X-ray excitation is defined as for CR-ray excitation.

In Table 4.5 we have gathered a few data on the several efficiencies of luminescent materials known to be efficient. These data were measured at room temperature [12]. The factors which restrict the photoluminescence efficiency, viz. the radiationless processes, were discussed above. For high-energy excitation, like cathode-ray or X-ray excitation, the situation is more complicated. Data like those presented in Table 4.5 for η_{CR} and n_X suggest that the maximum values of the radiant efficiency for host lattice excitation are restricted to values in between 10 and 20%. This in fact is the case. This observation has already drawn attention decades ago, and early explanations were offered in the sixties. The most detailed one is that by Robbins [13]. The next paragraph presents a summary of this work.

Vizio EX1018 Page 0095

Table 4.5. Efficiencies of some luminescent materials at room temperature after Ref. [12]. See also text (Sect. 4.3)

Luminescent material	η^a (%)	q^a (%)	L^a (lm/W)	$\eta_{CR}{}^b$ (%)	$\eta_X{}^c$ (%)
$MgWO_4$	44	84	115		
$Ca_5(PO_4)_3(F,Cl):Sb,Mn$	34	71	125		
$Zn_2SiO_4:Mn$ 6	35	70	175		
$CaWO_4$				3	6.5
$ZnS:Ag$				21	~ 20
$Gd_2O_2S:Tb$				11	13

[a] 250-270 nm excitation
[b] cathode-ray excitation
[c] X-ray excitation

4.4 Maximum Efficiency for High Energy Excitation [13]

In this section we will consider those types of exciting radiation which create many electrons and holes in the luminescent material under consideration. This type of excitation is usually indicated as high energy ionizing radiation. The most well-known examples are cathode rays and X rays, but one can also think of γ rays and α particles. It is usually assumed that the excitation process proceeds as follows:

The fast particle is absorbed in the lattice and creates secondary electrons and holes by ionization. One initial particle with high energy may create many electron-hole pairs. In $CaWO_4$, for example, one X-ray quantum may yield 500 quanta of emission. However, the fast particle and the created charge carriers may loose energy to the lattice by exciting vibrations. In order to create the average electron-hole pair (of energy E_g) a much larger amount of energy is needed. Long ago Shockley estimated this amount to be $3E_g$ for semiconductors, i.e. the maximum possible conversion efficiency is on this ground reduced to $\frac{1}{3}$.

More generally we can write for the average energy required to create an electron-hole pair

$$E = \beta E_g. \tag{4.4}$$

Robbins [13] showed that β can even be larger than 3. The dependence of β on the so-called energy loss parameter K is given in Figure 4.11. The K parameter is given by

$$K \sim (\varepsilon_\sim^{-1} - \varepsilon_s^{-1})(h\nu_{LO})^{3/2}(1.5\ E_g)^{-1}. \tag{4.5}$$

Here $\varepsilon_\sim$ is the high-frequency dielectric constant, ε_s the static dielectric constant, and ν_{LO} the frequency of the longitudinal optical vibration mode. The values of β range from about 3 (GaP, ZnS, CsI, NaI), via 4(La_2O_2S), 5.6 ($Y_3Al_5O_{12}$), to 7 ($CaWO_4$, YVO_4).

Vizio EX1018 Page 0096

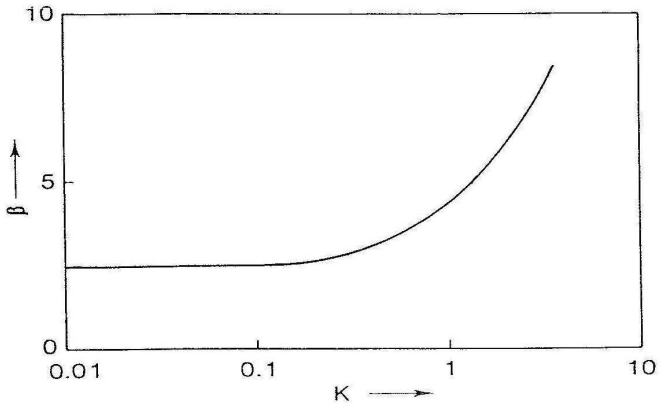

Fig. 4.11. The dependence of $\beta(= E/E_g)$ on the energy loss parameter K, defined in Eq. (4.5). See also text

The total expression for the radiant effiency looks as follows

$$\eta = (1 - r).\frac{h\nu_e}{E}.S.q. \tag{4.6}$$

Here r is the amount of radiation which is not absorbed, ν_e is the (averaged) frequency of the emitted radiation, E is defined by Eq. (4.4), S is the efficiency of transfer of electron-hole pair energy to the luminescent centre, and q is the quantum efficiency of the luminescent centre,

Assuming that all excitation energy is absorbed (i.e. $r = 0$), that all electron-hole pair energy arrives at the luminescent center (i.e. $S = 1$), and that $q = 100\%$, we arrive at the maximum radiant efficiency η_{max}:

$$\eta_{max} = h\nu_e E^{-1} = \frac{h\nu_e}{\beta E_g}. \tag{4.7}$$

The factor $h\nu_e$ accounts for the fact that the emitted energy will be less than the band gap energy. For example, in the case of ZnS : Ag $h\nu_e = 2.75$ eV and $E_g = 3.8$ eV, in the case of NaI : Tl 3.02 and 5.9, and of La_2O_2S : Eu 2.0 and 4.4, respectively. In this way the following η_{max} values can be calculated: $CaWO_4$ 8%, ZnS : Ag 25%, and $Gd_2O_2S : Tb^{3+}$ 15%. The experimental values (see Table 4.5) are close to these values.

This discussion shows that high values of η_{max} may be expected if the optical vibrational modes are at low frequency (i.e. low β), and the emission is close to the band gap energy.

4.5 Photoionization and Electron-Transfer Quenching

In this section we will draw attention to another type of radiationless transition, viz. that as a consequence of photoionization. In some cases the luminescence of a center

Vizio EX1018 Page 0097